Manuscript submitted to *EarthArXiv* as a non-peer-reviewed preprint
and also submitted for peer review to *Earth, Planets and Space*

Title page:

Title: Deep-learning-based denoising and interpolation of small displacements caused by fault slip using InSAR and GNSS data: Application to the 2019 M_w 6.2 Hyuga-nada earthquake

Author #1: Yutaro Okada, International Research Institute of Disaster Science, Tohoku University, Graduate School of Science, Tohoku University, yutaro.okada.c8@tohoku.ac.jp

Author #2: Yo Fukushima, International Research Institute of Disaster Science, Tohoku University, Graduate School of Science, Tohoku University, yo.fukushima.c3@tohoku.ac.jp

Corresponding author: Yutaro Okada

(go to new page)

Abstract

In recent years, deep learning techniques have become important tools in Solid Earth science, including geodesy. Previous studies have applied deep learning techniques to synthetic aperture radar interferometry (InSAR) or Global Navigation Satellite System (GNSS) data, which are two major observation techniques of satellite geodesy, to mitigate noise or detect small signals. Because InSAR and GNSS are complementary techniques, a deep-learning-based joint analysis can provide more detailed information. In this study, we developed a deep learning model that reproduces three-dimensional displacement fields from multiple interferograms and daily GNSS time series with gaps in the spatial and/or temporal domains. We employed a convolutional neural network-based architecture and trained the model using a synthetic dataset generated from signals from interplate slip and noise from multiple sources. Synthetic test results show that the developed model reproduces the ground truth with a variance reduction of greater than 60% when the maximum displacement amplitude exceeds 2 mm, although the performance depended on the noise level of the original GNSS data. We then applied our model to real InSAR and GNSS datasets of the coseismic displacements of the 2019 M_w 6.2 Hyuga-nada megathrust earthquake. The application successfully produced continuous displacement fields while suppressing incoherent random noise. The horizontal location of the rectangular fault model was consistent with the seismologically determined epicenter of the earthquake. Our results demonstrate the potential of deep learning techniques for obtaining denoised full displacement fields by combining multiple types of datasets.

Keywords

Deep learning, InSAR, GNSS, earthquakes, Convolutional neural network

Main Text

1 Introduction

Analyses of crustal deformation associated with fault slip are important for revealing the kinematic properties and stress accumulation/release history of faults. Space geodesy techniques have been major contributors to our understanding of crustal deformation since the 1990s (e.g., Massonnet et al. 1993; Shen et al. 1996; Heki et al.

1997; Burgmann 2002; Fialko 2006). The number of stations for Global Navigation Satellite System (GNSS) observations has increased as the cost of antennas and receivers has decreased. The number of satellites equipped with synthetic aperture radar (SAR) has also increased as their effectiveness for geoscience and hazard assessment has become increasingly recognized. Furthermore, a joint analysis of GNSS and SAR data enables more detailed information about fault slip to be extracted because they are complementary observations with different spatiotemporal sampling intervals (e.g., Delouis et al. 2002; Wang and Fialko 2018).

Since the 2000s, researchers have attempted to capture small transient signals from GNSS data, particularly those associated with slow slip events (SSEs) in subduction zones. Regression analysis and template matching techniques (e.g., Nishimura et al. 2013; Rousset et al. 2017; Okada et al. 2022; Yano and Kano 2022) have detected displacements with amplitudes approximately equal to the noise level of GNSS data, and have been widely applied to datasets along the Pacific Rim (e.g., Rousset et al. 2019; Okada and Nishimura 2023; Jara et al. 2024). A signal decomposition technique based on independent component analysis (e.g., Gualandi et al. 2016) is also effective for detecting small spatially correlated signals (Michel et al. 2019; Park et al. 2023). Recently, deep learning techniques have been applied to small-signal extraction problems (Costantino et al. 2023, 2024; Xue and Freymueller 2023; Nakagawa et al. 2024; Tanaka et al. 2025). However, detecting small-amplitude signals whose characteristic spatial scales are smaller than the station spacing remains challenging.

Persistent deformation localized around inland faults, particularly long-term fault creep, has been successfully identified using SAR interferometry (InSAR) with millimeter-per-year accuracy (e.g., Jolivet et al. 2012; Lindsey et al. 2014; Okur et al. 2025). However, it had remained difficult to extract millimeter- to centimeter-scale transient signals with days-to-weeks duration from InSAR data because of its limited temporal resolution (Rousset et al. 2016; Molina-Ormazabal et al. 2025). Similar to GNSS, deep learning techniques have been employed for SAR data since the late 2010s (Zhu et al. 2021). In the context of signal extraction from InSAR data, Schwegmann et al. (2017) and Anantrasirichai et al. (2019a, b) detected line-of-sight (LOS) changes in single image using a convolutional neural network (CNN) based classifier. Rouet-Leduc et al. (2021) and Zhu et al. (2024) developed architectures that produce a denoised image from multiple noisy images under the framework of a CNN-based autoencoder. Their models successfully extracted millimeter-scale signals from observed InSAR images.

As described above, the approaches and techniques for extracting small transient signals have evolved independently for GNSS and InSAR data. However, these are complementary measurements, and joint use of InSAR and GNSS data should be able to improve the spatial and temporal resolutions. Therefore, in this study, we developed a new method that provides denoised and interpolated three-dimensional displacement fields from InSAR and GNSS data. We adopted a CNN-based autoencoder, which has been successful in previous studies dealing with satellite geodetic data (e.g., Rouet-Leduc et al. 2021; Zhu et al. 2024; Nakagawa et al. 2024; Tanaka et al. 2025). We first trained the model using synthetic datasets, which were generated assuming the megathrust slip in the Hyuga-nada region, the westernmost part of the Nankai subduction zone (Figure 1). Then, we evaluated the model performance using the synthetic test data. Finally, we applied the trained model to real InSAR and GNSS data with signals of the 2019 M_w 6.2 Hyuga-nada earthquake. We selected this test event for two reasons: (1) it produced moderate (~1 cm) displacements, which are easily detected by GNSS but challenging for InSAR, and (2) the feasibility of evaluating the application result based on an independent seismic observation.

2 Deep learning model and its training

2.1 Architecture of the deep learning model

Our model comprises three blocks: InSAR processing, GNSS processing, and integration of the two (Figure 2). In this section, we describe the input data types and the outline of the architecture of each block. See Figures S1 – S3 and Table S1 for further details.

2.1.1 InSAR processing block

The InSAR processing block receives a three-dimensional tensor composed of 24 interferograms, each comprising 46×46 pixels with a pixel spacing of 0.02° (Figure 2). We replaced the observed values at pixels with coherence lower than 0.1 with zeros.

We employed an architecture largely similar to that proposed by Rouet-Leduc et al. (2021), while adopting the input format used by Zhu et al. (2024). This block first performs three-dimensional convolutions. This part compresses the information in the time domain by max pooling, while retaining the size in the spatial domain by zero padding (Figure S1 and Table S1). After compression along the temporal dimension, we added a digital elevation map (DEM) as an additional feature map (Rouet-Leduc et al. 2021) (Figure 2). We then applied additional two-dimensional convolutions to suppress topography-correlated noise.

2.1.2 GNSS processing block

We treated the input GNSS data as images following Nakagawa et al. (2024); we inserted the displacement for each day into the pixels of a day-by-day image, whose size and pixel spacing were the same as those of the interferograms. The value at the pixel without GNSS stations was set to zero. By repeating this procedure from day -60 to day 60 (the time relative to the occurrence date of a target event), we obtained 121 GNSS position images. We aligned these images in time order for each component to form three tensors, each of size $121 \times 46 \times 46$, as the inputs of our CNN model (Figure 2).

We employed an architecture similar to that of the InSAR processing block for the GNSS processing block, with two modifications of the architecture (Figure S2). First, we adopted a larger kernel size in the spatial domain to efficiently connect pixels with nonzero values, which are sparser in GNSS images than in InSAR data (Figures S1 and S2). Second, we omitted the DEM addition process under the assumption that the topography-correlated noise in the GNSS data is negligible.

2.1.3 Joint processing block

In this block, we concatenated the feature maps from the preceding two blocks and conducted two-dimensional convolutions to decode the three-dimensional displacement fields (Figures 2 and S3). This concatenation enables effective reconstruction of the three-dimensional displacement field by mitigating the limitations and noise characteristics inherent to each observation technique.

2.2 Generation of synthetic data for training

2.2.1 Ground truth displacement fields

We assumed a rectangular fault (Okada 1992) on the Philippine Sea plate (Iwasaki et al. 2015) as the dislocation source for the ground-truth displacement fields (Figure 3a), based on the centroid moment tensor (CMT) solution of the target event. To train our model using various ground truths, we prepared 77,112 fault models by varying the fault-center longitude and latitude, aspect ratio α, stress drop $\Delta\sigma$, slip direction ϕ, and moment magnitude M_w. We define α as

$$\alpha = \frac{L}{W}, \tag{1}$$

where L and W represent the length and width of the fault plane, respectively. For stress drop $\Delta\sigma$, we adopt the definition of Ohno et al. (2021), that is,

$$\Delta\sigma = \frac{\mu D}{\sqrt{LW}}, \tag{2}$$

where μ and D are the rigidity and the slip magnitude, respectively. In this study, we assume a rigidity of 40 GPa. Given the definition of moment magnitude

$$\mathrm{M_w} = \frac{\log_{10}(\mu DLW) - 9.1}{1.5}, \tag{3}$$

the length L, width W, and slip magnitude D are uniquely determined by assuming the aspect ratio α, stress drop $\Delta\sigma$, and moment magnitude. The slip direction ϕ is defined as:

$$\phi = \varphi - \lambda, \tag{4}$$

where φ and λ are the strike and rake angles, respectively (e.g., Nishimura et al. 2013). The depth, strike, and dip were determined based on the geometry of the slab interface (Iwasaki et al. 2015) around the fault center (e.g., Nishimura et al. 2013). The parameter ranges are listed in Table S2 and were selected based on regional tectonics (DeMets et al. 2010). Finally, we assigned a step function to represent the temporal evolution of the target signals.

2.2.2 Synthetic noise in InSAR data

In this study, we generated four types of synthetic noise assumed to be present in InSAR data.

We first generated topography-correlated noise, which is caused by radar signal delay owing to the stratified component of the troposphere (e.g., Fujiwara et al. 1999; Doin et al. 2009). Using the Shuttle Radar Topography Mission (SRTM) DEM (Farr et al. 2007), we calculated the apparent displacement $d_{i,j}^{topo}$ at jth pixel (in mm) owing to the ith topography-correlated noise under a simple linear relation between the SRTM height h_j (in m) and displacement $d_{i,j}^{topo}$, that is,

$$d_{i,j}^{topo} = \mathrm{sign}\left(a_i^{topo}\right) b_i^{topo} h_j, \tag{5}$$

where a_i^{topo} and b_i^{topo} are random numbers that determine the sign and amplitude of the noise, respectively. In this study, a_i^{topo} and b_i^{topo} followed a uniform distribution $U(-1,1)$ and Gaussian distribution $\mathcal{N}(0.05, 0.01^2)$ (in mm), respectively. The parameters used to generate the noise amplitude were determined based on a previous study conducted around Mt. Fuji (Ozawa and Shimizu 2010).

The second component is the long-wavelength noise $d_{i,j}^{lw}$ (in mm), which is typically caused by ionospheric and tropospheric delays. We model this noise as a simple plane, expressed as

$$d_{i,j}^{lw} = a_i^{lw} x_j + b_i^{lw} y_j, \tag{6}$$

where x_j and y_j are the coordinates of the jth pixel in the local Cartesian coordinate system (in km), whose origin is at the center of the image. Here, the amplitude a_i^{lw} and b_i^{lw} follow a Gaussian distribution $\mathcal{N}(0.0, 0.5^2)$ independently.

The third component is the spatially-correlated random noise $d_{i,j}^{sc}$, which is typically attributed to tropospheric delay. It is assumed to follow a multivariate Gaussian distribution $\mathcal{N}(\boldsymbol{O}, \boldsymbol{C}_i^{sc})$. Here, the (j,k) element of $\boldsymbol{C}_i^{sc}$ is defined as

$$C_{j,k}^{sc} = a_i^{sc} \exp\left(\frac{r_{j,k}}{b_i^{sc}}\right), \tag{7}$$

where $r_{j,k}$ is the distance between the jth and kth pixels. The coefficients a_i^{sc} (unit: mm) and b_i^{sc} (unit: km) follow uniform distributions $U(2.1^2, 22.1^2)$ and $U(0.93, 17.70)$, respectively. These ranges were selected based on the study by

Ghayournajarkar and Fukushima (2022). After preparing the three noise components, we created interferogram-independent noise $d_{i,j}^{ii}$ as

$$d_{i,j}^{ii} = d_{i,j}^{topo} + d_{i,j}^{lw} + d_{i,j}^{sc}. \quad (8)$$

Finally, we generated an interferogram-dependent decorrelation noise $d_{i,j,l}^{dc}$ for the lth interferogram. To determine the appropriate range for this noise, we calculated the standard deviation of the unwrapped displacement $\sigma_{j,l}^{dc}$ and the average coherence $\gamma_{j,l}$ of pixels in 5×5 pixel moving windows from the real interferograms processed in the target region (Lazecký et al. 2020) (see section 4.2.1 in details). Because the resulting relationship between these values appeared to follow an exponential trend (Figure S4), we adopted the following empirical relationship

$$\sigma_{j,l}^{dc} = 2.168\exp\left(-12.25\gamma_{j,l} + 1.196\right) + 0.4826, \quad (9)$$

where the constants were estimated using a nonlinear least-squares method. We generated the ith decorrelation noise $d_{i,j,l}^{dc}$ at the jth pixel of the lth interferogram by sampling from a Gaussian distribution $\mathcal{N}(0.0, {\sigma_{j,l}^{dc}}^2)$.

We prepared 2,000 patterns of $d_{i,j}^{ii}$ and 2,000 patterns of $d_{i,j,l}^{dc}$ for 24 interferograms. Finally, the synthetic InSAR noise pattern $d_{i,j,l}^{SAR}$ was generated by randomly combining the prepared noise components

$$d_{i,j,l}^{SAR} = d_{m,j}^{ii} + d_{m,j,l}^{dc}, \quad (10)$$

where m is an integer between 1 and 2,000 that follows a uniform distribution.

2.2.3 Synthetic noise in GNSS data

We assumed that noise in the GNSS time series can be represented as the sum of Gaussian and random-walk noise. For the horizontal components, we generated synthetic noise using a Gaussian distribution $\mathcal{N}(0.0, 2.0^2)$ (unit: mm) and a random-walk with a scale parameter of 1 mm/yr$^{1/2}$ (Fukuda et al. 2008; Okada and Ueda 2025). For the vertical component, we set the standard deviation of the Gaussian noise and the scale parameter of the random-walk noise to 5.0 mm and 2.5 mm/yr$^{1/2}$, respectively. These values were selected based on the statistics of the F5.0 position data provided by the Geospatial Information Authority of Japan (cf. Takamatsu et al. 2023). Given the above settings, we prepared 2,000 noise patterns for each component at 21 stations within the target area (Figure 4).

2.3 Training of the deep learning model

We generated 200,000 datasets with different combinations of the ground truth, InSAR noise, and GNSS noise. We split them into training and validation sets at a ratio of 8:2. We trained our model on the training dataset using mini-batch training with a batch size of 64. For the loss function $\mathcal{L}$, we used the mean-squared error defined as

$$\mathcal{L} = \frac{1}{3N}\sum_{i=1}^{3}\sum_{j=1}^{N}\left(G_{i,j} - I_{i,j}\right)^2, \tag{11}$$

where $G_{i,j}$ and $I_{i,j}$ denote the ground truth and inferred displacements of the ith component at the jth pixel, respectively. In this study, N = 2,116. We minimized $\mathcal{L}$ by employing the Adam optimizer (Kingma and Ba 2017) with a learning rate of 0.01. We conducted the training process for 100 epochs and adopted the parameters from the final epoch (Figure S5). Although the fluctuations in the validation loss may suggest overfitting, the trained model is considered to have sufficient generalization performance within the assumed synthetic-data distribution because the square root of the validation loss is substantially smaller than the noise level of the observed GNSS data.

3 Investigation of model characteristics using synthetic data

3.1 Model performance

First, we applied the trained model to 10,000 synthetic test cases to evaluate its performance. We used variance reduction (VR) as the evaluation metric, calculated for the ith component as follows:

$$\mathrm{VR}_i = \left(1 - \frac{\sum_{j=1}^{N}\left(G_{i,j} - I_{i,j}\right)^2}{\sum_{j=1}^{N} G_{i,j}^2}\right) \times 100. \tag{12}$$

Here, we present two typical cases: large (> 2 cm) and small (a few to several millimeters) maximum ground truth displacements. In the large displacement case, our model successfully reproduced the ground truth with VR values of 98.8, 84.0, and 97.0% for east-west (EW), north-south (NS), and up-down (UD) components, respectively (Figure S6), despite the high noise level in the InSAR dataset (Figure S7). In the small displacement case, our model also reproduced the ground truth with VR values of 82.5, 91.2, and 95.4% for EW, NS, and UD components, respectively, even when the maximum amplitudes of the ground truth were 2.4, 2.8, and 8.6 mm for EW, NS, and UD components (Figure 5), and the noise was dominant in the input interferograms (Figure S8).

To investigate the general performance of our model, we examined the distribution of the VRs with respect to the maximum amplitude of the ground truth image (Figure 6). For all components, our model reproduced the ground truth with VRs greater than

90% when the maximum amplitude of the ground truth was greater than 1 cm. In the range between 1 mm and 1 cm, the model performance for the horizontal components was better than that for the vertical component. This was probably due to the difference in the assigned noise level between the horizontal and vertical components of the GNSS data. In addition, the maximum displacement corresponding to a mean VR was 80% was roughly consistent with the noise level of each GNSS component. These results suggest that the performance of our model is primarily controlled by the noise levels of the GNSS data.

3.2 Contribution of each data type

To investigate the relative contribution of each data type, we developed an alternative model using only GNSS data (hereafter, GNSS-only model), whose architecture is mostly the same as the "GNSS processing block" in the model presented in the previous section (hereafter, the joint model) (Figure S9). We trained the model using the same dataset and strategy as those used in the training of the joint model (Sections 2.2 and 2.3).

We applied the joint and GNSS-only models to the same 10,000 test cases and compared the VR curves for each model (Figure 7). In cases with a maximum displacement between 1 mm and 1 cm, the VR curves of EW and UD components exhibited similar features. However, for the NS component, the VRs of the joint model were higher than those of the GNSS-only model. This can be attributed to the fact that reverse slip on a fault located away from the observation points tends to cause complex displacement patterns in the fault-parallel displacement field, which approximately corresponds to the NS component in the target region, compared with the fault-perpendicular (approximately EW) component (Figure S10). We suggest that the spatially dense InSAR data effectively contributed to the interpolation of such complex displacement fields.

4 Application to the 2019 M_w 6.2 Hyuga-nada earthquake

4.1 Seismotectonics of the Hyuga-nada region, southwest Japan

The Philippine Sea plate subducts beneath the Amurian plate at a rate of 63–68 mm/yr in the Nankai subduction zone, southwest Japan (Figure 1) (Miyazaki and Heki 2001). The Hyuga-nada region, which lies in the southernmost part of the Nankai subduction zone and has a complex slab interface shape due to the subduction of the

Kyushu-Palau Ridge, hosts abundant ordinary earthquakes and slow earthquakes. In 1996, an M 6.7 doublet occurred on the megathrust (Yagi et al. 1999). More recently, the megathrust hosted a similar doublet in August 2024 and January 2025 (e.g., Itoh, 2025; Shibata et al. 2025; Zhang et al. 2025). Significant afterslips have occurred after both doublets (e.g., Yagi et al. 2001; Itoh 2025). In the downdip portion of the megathrust seismogenic zone, years-long and weeks-long slow slips have been reported based on GNSS observations (e.g., Yarai and Ozawa 2013; Nishimura 2014). Shallow tectonic tremors and very-low-frequency earthquakes have also been detected updip of the seismogenic zone through onshore and offshore seismic observations (Asano et al. 2015; Yamashita et al. 2015).

The 2019 Hyuga-nada earthquake occurred on May 9, 2019, and its CMT solution, estimated by the Japan Meteorological Agency (JMA), indicated reverse faulting with M_w 6.2 (Figure 1). The Disaster Prevention Research Institute, Kyoto University (2019) reported that up to ~1 cm of coseismic displacement was recorded at onshore GNSS stations in the southern Kyushu region.

4.2 Preparation of InSAR and GNSS data

Although one of the features of our deep learning model is the denoising of geodetic data, we performed noise removal on the datasets before applying our model. The motivation for this preprocessing was to remove components that were not included in the synthetic data generation, such as seasonal oscillations and common-mode errors in the GNSS data.

4.2.1 InSAR data

We used 24 descending interferograms of the Sentinel-1 satellite for which the acquisition dates of the primary and secondary images were within ±60 days of the earthquake. We retrieved the interferograms provided by LiCSAR (Lazecký et al. 2020) and analyzed them using the LiCSBAS software (Morishita et al. 2020). We resampled the interferograms with a pixel spacing of 0.02° to match the spatial extent and resolution of the synthetic datasets. We then applied the Generic Atmospheric Correction Online Service (Yu et al. 2018) to reduce the tropospheric delay component.

4.2.2 GNSS data

We used the daily positions of 273 GNSS stations (Figure S11) between January 1, 2017, and December 31, 2021, provided by the Geospatial Information Authority of

Japan. These were estimated based on the F5 strategy (Takamatsu et al. 2023) and were aligned with the International Terrestrial Reference Frame 2014 (Altamimi et al. 2016).

We preprocessed the GNSS displacement time-series as follows. First, we estimated offsets associated with station maintenance by fitting a linear and step function to data points within ±30 epochs of the maintenance, and removed offsets from the entire time series. Second, we calculated the daily relative displacements with respect to a reference station 950459 (Figures S11 and S12). Third, we applied the seasonal-trend-episodic decomposition procedure based on Loess (STEL) (Okada and Ueda 2025) to remove seasonal oscillations. For the episodic component estimation, we estimated coseismic steps for each moderate earthquake (Table S3) using the aforementioned functional model fitted to data within ±30 days of the target earthquake. We then summed the estimated step functions. Fourth, we calculated the common-mode errors by employing a spatial filter (Wdowinski et al. 1997) on the remainder component of the STEL result and removed them from the deseasonalized time series (Figure S12). Finally, we extracted the data for the 21 stations in the period within ±60 days of the 2019 Hyuga-nada earthquake and removed the short-term linear trend component estimated by fitting a linear trend and a step function to data from days -60 to -21 and days 21 to 60 relative to the earthquake.

4.3 Application of the deep learning model

We applied our deep learning model to the preprocessed InSAR and GNSS data (Figures S13 and S14), and obtained denoised and interpolated displacement fields for the EW, NS, and UD components (Figure 8). The estimated displacement fields were spatially smooth, without short-wavelength noise patterns.

As a consistency check, we compared the displacements computed directly from the preprocessed GNSS data with the estimated displacements at the pixels containing the GNSS stations (Figure S15). This comparison focuses on GNSS data because its three-dimensional, point-based measurements allow for a more direct and clear validation of each displacement component than InSAR data. The GNSS displacements were calculated as the difference between the average positions from April 29 to May 8, 2019, and from May 10 to 11, 2019. The uncertainty of each GNSS displacement was defined as the square root of the sum of variances in the two aforementioned periods. The horizontal displacements estimated by the deep learning model were consistent with the observation within the 68% confidence interval (Figure S15a). However, the random pattern in the vertical displacements calculated directly from the time series was suppressed in the deep learning result. This may indicate effective noise reduction by our model.

4.4 Source model estimation

To evaluate the effectiveness of our denoising and interpolation for the source modeling, we estimated a rectangular source model for the 2019 Hyuga-nada earthquake using the displacement fields produced by our model.

4.4.1 Inversion strategy

The observation equation is defined as follows:

$$\boldsymbol{u} = \boldsymbol{G}(\boldsymbol{\theta}^f) + \boldsymbol{\Gamma}\boldsymbol{\theta}^t + \boldsymbol{\varepsilon}, \tag{13}$$

where $\boldsymbol{u}$ denotes the horizontal and vertical displacements at stations or pixels. The parameter vector $\boldsymbol{\theta}^f$ characterizes the rectangular fault, and the function $\boldsymbol{G}(\cdot)$ converts $\boldsymbol{\theta}^f$ to displacements $\boldsymbol{u}$ (Okada 1992). The parameter vector $\boldsymbol{\theta}^t$ denotes the three-dimensional translational displacement, and $\boldsymbol{\Gamma}$ is a matrix that calculates the translational displacements. The vector $\boldsymbol{\varepsilon}$ denotes observational errors, which are assumed to follow a Gaussian distribution $\mathcal{N}(\boldsymbol{O}, \boldsymbol{E})$. To estimate the diagonal components of $\boldsymbol{E}$, we computed the truncated mean of the squared residual of the 10,000 applications of our deep learning model to synthetic data, with $\pm 5\%$ trimming (Figures S16 and S17).

We adopted a grid search approach (e.g., Okada and Nishimura 2025) to avoid convergence to local minima. Each iteration of our grid-search approach comprised the following three steps:

Step 1: Define a set of fault-associated parameter values for $\boldsymbol{\theta}^f$ based on a combination of fault-center longitude and latitude, width W, aspect ratio α, moment magnitude $\mathrm{M_w}$, and rake λ. The depth, strike φ, and dip are calculated from the longitude, latitude, and the slab surface geometry (Iwasaki et al. 2015). The length L and slip D are computed based on width W, aspect ratio α, and moment magnitude $\mathrm{M_w}$ using Equations (1) and (3).

Step 2: Estimate $\boldsymbol{\theta}^t$ by a weighted linear least-squares method using residual displacements from those associated with a fault slip, that is,

$$\boldsymbol{\theta}^t = (\boldsymbol{\Gamma}^T \boldsymbol{E}^{-1} \boldsymbol{\Gamma})^{-1} \boldsymbol{\Gamma}^T \boldsymbol{E}^{-1} \{\boldsymbol{u} - \boldsymbol{G}(\boldsymbol{\theta}^f)\}, \tag{13}$$

where T and -1 denote transpose and inverse of a matrix, respectively.

Step 3: Evaluate the selected $\boldsymbol{\theta}^f$ and $\boldsymbol{\theta}^t$ based on the chi-squared statistic χ^2, that is,

$$\chi^2 = \{\boldsymbol{u} - \boldsymbol{G}(\boldsymbol{\theta}^f) - \boldsymbol{\Gamma}\boldsymbol{\theta}^t\}^T \boldsymbol{E}^{-1} \{\boldsymbol{u} - \boldsymbol{G}(\boldsymbol{\theta}^f) - \boldsymbol{\Gamma}\boldsymbol{\theta}^t\}. \tag{14}$$

To summarize, we performed a grid search for six parameters associated with the rectangular fault (Table S4). For each candidate set of $\boldsymbol{\theta}^f$, the translation vector $\boldsymbol{\theta}^t$ was analytically estimated using the weighted linear least-squares method. We then selected the combination of $\boldsymbol{\theta}^f$ and $\boldsymbol{\theta}^t$ that minimized χ^2.

4.4.2 Estimated source model

The estimated source model successfully reproduced the input displacements denoised by the deep learning model (Figure 9). For all components, the residuals at offshore pixels were larger than those at onshore pixels (Figures 9g–i), which is consistent with the large uncertainty for the model output (Figure S16).

We compared the magnitude and the horizontal source location of the estimated source model with the JMA CMT solution to assess its validity. The estimated seismic moment was 7.08×10^{18} Nm with a rigidity of 40 GPa, corresponding to M_w 6.5. The estimated moment was ~2.8 times that of the JMA CMT solution (2.51×10^{18} Nm). The difference may partly reflect factors unrelated to the deep learning application, such as the differences in rigidity and constraints on the source depth. In addition, such a discrepancy is not uncommon and is therefore not considered significant here (Weston et al., 2011). Therefore, we suggest that the difference in the estimated magnitude is probably caused by the inversion strategy and dataset and does not substantially affect the evaluation of the capability of the deep learning model. On the other hand, the estimated fault model was located within 10 km of the JMA CMT solution (Figure 10). Given these comparisons, we conclude that the deep learning model successfully extracted reasonable coseismic signals consistent with the seismologically estimated source model.

The estimated source model lies near the updip limit of the seismogenic zone of the megathrust, which is close to the tremorgenic zone (Yamashita et al. 2021) (Figure 10).

The 2019 earthquake was spatially separated from the large-slip areas of the M 6.5+ megathrust earthquakes, particularly the 2024 M_w 7.0 Hyuga-nada earthquake (Itoh 2025). This separation might suggest a complex distribution of asperities potentially hosting M 6+ earthquakes on the megathrust in the Hyuga-nada region, although the inference of asperity distribution requires further investigation.

5 Conclusions and future perspectives

In this study, we developed a CNN-based deep learning model that denoises and interpolates InSAR and GNSS data. The fault model estimated using the output of the CNN model was consistent with the CMT model estimated using a seismic dataset. These results suggest that deep learning models can effectively extract and integrate information from InSAR and GNSS data.

Although we demonstrated the substantial potential of deep learning applications to multiple types of geodetic datasets, the proposed model still has room for improvement. For example, we developed the model for a specific number of InSAR inputs, but a model that can be applied without specifying a fixed number of interferograms would be useful for continuous monitoring of slip behavior in megathrusts and crustal faults.

Furthermore, although we employed a simple CNN-based architecture, more advanced techniques, such as Transformer-based architectures (Vaswani et al. 2025), may enable the detection of smaller signals. The use of improved approaches and advanced techniques may enable us to achieve state-of-the-art geodetic monitoring and modeling. Finally, our results demonstrate the advantage of the joint analysis of InSAR and GNSS data via deep learning techniques for displacement fields containing both short- and long-wavelength signals, particularly for components or spatial patterns that are difficult to interpolate from sparse GNSS data alone. We believe that our approach may be more effective for transient signal detection on inland faults, where short-wavelength deformation is expected.

List of abbreviations

CMT: Centroid Moment Tensor

CNN: Convolutional Neural Network

DEM: Digital Elevation Map

EW: East-West

GEONET: Global navigation satellite system Earth Observation NETwork system

GNSS: Global Navigation Satellite System

InSAR: Synthetic Aperture Radar Interferometry

JMA: Japan Meteorological Agency

LOS: Line-Of-Sight

NS: North-South

SAR: Synthetic Aperture Radar

SRTM: Shuttle Radar Topography Mission

SSE: Slow Slip Event

STEL: Seasonal-Trend-Episodic decomposition procedure based on Loess

UD: Up-Down

VR: Variance Reduction

Declarations

The authors *must* provide the following sections under the heading "Declarations".

Ethics approval and consent to participate

Not applicable

Consent for publication

Not applicable

Availability of data and materials

We used interferograms of Sentinel-1 satellite operated by European Space Agency and processed by LiCS (Lazecký et al. 2020) (https://comet.nerc.ac.uk/comet-lics-portal/) and F5.0 daily positions (Takamatsu et al. 2023) of GEONET stations (Geodetic Observation Center, Geospatial Information Authority of Japan, 2025). The trained models and scripts required to reproduce this study are published online archive (Okada & Fukushima, 2026).

Competing interests

The authors declare that they have no competing interests.

Funding

This work was supported by the Uehiro Foundation on Ethics and Education, JSPS (Japan Society for the Promotion of Science) KAKENHI (Grant Number: JP23KJ1184 and JP24K07165), and the

MEXT (Ministry of Education, Culture, Sports, Science and Technology) Project for Seismology toward Research Innovation with Data of Earthquake (STAR-E) (Grant Number: JPJ010217).

Authors' contributions

YO and YF designed this study. YO developed deep learning models, analyzed data, conducted the inversions, and wrote the first version of the manuscript. YF supervised YO and improved the manuscript.

Acknowledgements

Discussions with Drs. Masayuki Kano, Keisuke Yano, and Weiqiang Zhu were fruitful. The plate model by Iwasaki et al. (2015) was constructed from topography and bathymetry data by Geospatial Information Authority of Japan (250-m digital map), Japan Oceanographic Data Center (500m mesh bathymetry data, J-EGG500, http:// www. jodc. go. jp/ jodcw eb/ JDOSS/ infoJEGG_j. html) and Geographic Information Network of Alaska, University of Alaska (Lindquist et al., 2004).

Authors' information

Affiliations

International Research Institute of Disaster Science, Tohoku University, 468-1 Aoba, Aramaki, Aoba-ku, Sendai 980-8572, Japan.

Graduate School of Science, Tohoku University, Aramaki Aza-Aoba 6-6, Aoba-ku, Sendai, 980-8578, Japan

Yutaro Okada

International Research Institute of Disaster Science, Tohoku University, 468-1 Aoba, Aramaki, Aoba-ku, Sendai 980-8572, Japan.

Graduate School of Science, Tohoku University, Aramaki Aza-Aoba 6-6, Aoba-ku, Sendai, 980-8578, Japan

Yo Fukushima

Endnotes

We do not have any endnotes.

References

Altamimi Z, Rebischung P, Métivier L, Collilieux X (2016) ITRF2014: A new release of the International Terrestrial Reference Frame modeling nonlinear station motions. J Geophys Res Solid Earth 121:6109–6131. https://doi.org/10.1002/2016JB013098

Anantrasirichai N, Biggs J, Albino F, Bull D (2019a) A deep learning approach to detecting volcano deformation from satellite imagery using synthetic datasets. Remote Sens Environ 230, 111179. https://doi.org/10.1016/j.rse.2019.04.032

Anantrasirichai N, Biggs J, Albino F, Bull D (2019b) The application of convolutional neural networks to detect slow, sustained deformation in InSAR time series. Geophys Res Lett 46:11850–11858. https://doi.org/10.1029/2019GL084993

Asano Y, Obara K, Matsuzawa T, Hirose H, Ito Y (2015) Possible shallow slow slip events in Hyuga-nada, Nankai subduction zone, inferred from migration of very low frequency earthquakes. Geophys Res Lett 42:331–338. https://doi.org/10.1002/2014GL062165

Bürgmann R, Ayhan ME, Fielding EJ, Wright TJ, McClusky S, Aktug B, Demir C, Lenk O, Türkezer A (2002) Deformation during the 12 November 1999 duzce, turkey, earthquake, from GPS and InSAR data. Bull Seismol Soc Am 92:161–171. https://doi.org/10.1785/0120000834

Costantino G, Giffard-Roisin S, Mura MD, Socquet A (2024) Denoising of geodetic time series using spatiotemporal graph neural networks: Application to slow slip event extraction. IEEE J Sel Top Appl Earth Obs Remote Sens 17:17567–17579

Costantino G, Giffard-Roisin S, Radiguet M (2023) Multi-station deep learning on geodetic time series detects slow slip events in Cascadia. Commun Earth

Environ 4, 435. https://doi.org/10.1038/s43247-023-01107-7

Delouis B, Giardini D, Lundgren P, Salichon J (2002) Joint inversion of InSAR, GPS, teleseismic, and strong-motion data for the spatial and temporal distribution of earthquake slip: Application to the 1999 izmit mainshock. Bull Seismol Soc Am 92:278–299. https://doi.org/10.1785/0120000806

DeMets C, Gordon RG, Argus DF (2010) Geologically current plate motions. Geophys J Int 181:1–80. https://doi.org/10.1111/j.1365-246X.2009.04491.x

Disaster Prevention Research Institute, Kyoto University (2019) Crustal deformation associated with the M6.3 Hyuganada earthquake observed by GNSS. Reports of the Coordinating Committee for Earthquake Prediction, Japan(Report No. 102, pp. 326–328). Retrieved from https://cais.gsi.go.jp/YOCHIREN/report/kaihou102/09_06.pdf (In Japanese)

Doin M-P, Lasserre C, Peltzer G, Cavalié O, Doubre C (2009) Corrections of stratified tropospheric delays in SAR interferometry: Validation with global atmospheric models. J Appl Geophy 69:35–50. https://doi.org/10.1016/j.jappgeo.2009.03.010

Farr TG, Rosen PA, Caro E, Crippen R, Duren R, Hensley S, Kobrick M, Paller M, Rodriguez E, Roth L, et al (2007) The shuttle radar topography mission. Rev Geophys. https://doi.org/10.1029/2005RG000183

Fialko Y (2006) Interseismic strain accumulation and the earthquake potential on the southern San Andreas fault system. Nature 441:968–971. https://doi.org/10.1038/nature04797

Fujiwara S, Tobita M, Murakami M, Nakagawa H, Rosen PA (1999) Baseline determination and correction of atmospheric delay induced by topography of SAR interferometry for precise surface change detection. Journal of the Geodetic Society of Japan 45:315–325. https://doi.org/10.11366/sokuchi1954.45.315

Fukuda J, Miyazaki S, Higuchi T, Kato T (2008) Geodetic inversion for space—time distribution of fault slip with time-varying smoothing regularization. Geophys J

Int 173:25–48. https://doi.org/10.1111/j.1365-246X.2007.03722.x

Geodetic Observation Center, Geospatial Information Authority of Japan (2025) GNSS data. Geospatial Information Authority of Japan. https://doi.org/10.57499/GSI_GNSS_2025_001

Ghayournajarkar N, Fukushima Y (2022) Using InSAR for evaluating the accuracy of locations and focal mechanism solutions of local earthquake catalogues. Geophys J Int 230(1):607–622. https://doi.org/10.1093/gji/ggac072

Gualandi A, Serpelloni E, Belardinelli ME (2016) Blind source separation problem in GPS time series. J Geodesy 90:323–341. https://doi.org/10.1007/s00190-015-0875-4

Heki K, Miyazaki S, Tsuji H (1997) Silent fault slip following an interplate thrust earthquake at the Japan Trench. Nature 386:595–598. https://doi.org/10.1038/386595a0

Itoh Y (2025) Coseismic slip and early afterslip of the 2024 Hyuganada earthquake modulated by a subducted seamount. Geophys Res Lett 52:e2024GL112826. https://doi.org/10.1029/2024GL112826

Iwasaki T, Sato H, Shinohara M, Ishiyama T, Hashima A (2015) Fundamental structure model of island arcs and subducted plates in and around Japan. In: Abstract of 2015 Fall Meeting, American Geophysical Union, San Francisco, 14–18 December 2015.

Jara J, Jolivet R, Socquet A, Comte D, Norabuena E (2024) Detection of slow slip events along the southern Peru - northern Chile subduction zone. Seismica 3(1). https://doi.org/10.26443/seismica.v3i1.980

Jolivet R, Lasserre C, Doin M-P, Guillaso S, Peltzer G, Dailu R, Sun J, Shen Z-K, Xu X (2012) Shallow creep on the Haiyuan Fault (Gansu, China) revealed by SAR Interferometry. J Geophys Res 117:B06401. https://doi.org/10.1029/2011jb008732

Kingma DP, Ba J (2017) Adam: A Method for Stochastic Optimization. arXiv:1412.6980v9. https://doi.org/10.48550/arXiv.1412.6980

Lazecký M, Spaans K, González PJ, Maghsoudi Y, Morishita Y, Albino F, Elliott J, Greenall N, Hatton E, Hooper A, et al (2020) LiCSAR: An automatic InSAR tool for measuring and monitoring tectonic and volcanic activity. Remote Sens 12(15):2430. https://doi.org/10.3390/rs12152430

Lindsey EO, Fialko Y, Bock Y, Sandwell DT, Bilham R (2014) Localized and distributed creep along the southern San Andreas Fault. J Geophys Res: Solid Earth 119:7909–7922. https://doi.org/10.1002/2014JB011275

Lindquist KG, Engle K, Stahlke D, Price E (2004) Global topography and bathymetry grid improves research efforts. Eos Trans AGU 85(19):186. https://doi.org/10.1029/2004EO190003

Massonnet D, Rossi M, Carmona C, Adragna F, Peltzer G, Feigl K, Rabaute T (1993) The displacement field of the Landers earthquake mapped by radar interferometry. Nature 364:138–142. https://doi.org/10.1038/364138a0

Michel S, Gualandi A, Avouac J-P (2019) Interseismic Coupling and Slow Slip Events on the Cascadia Megathrust. Pure Appl Geophys 176:3867–3891. https://doi.org/10.1007/s00024-018-1991-x

Miyazaki S, Heki K (2001) Crustal velocity field of southwest Japan: Subduction and arc-arc collision. J Geophys Res 106(B3):4305–4326. https://doi.org/10.1029/2000JB900312

Molina-Ormazabal D, Radiguet M, Münchmeyer J, Hernandez-Soto N, Vezinet A, Pousse-Beltran L, Castro C, Doin M-P, Baez JC, Moreno M, et al (2025) Slip modes along a structurally ‐ driven earthquake barrier in Chile. J Geophys Res Solid Earth 130: e2024JB030796. https://doi.org/10.1029/2024jb030796

Morishita Y, Lazecky M, Wright TJ, Weiss JR, Elliott JR, Hooper A (2020) LiCSBAS: An Open-Source InSAR Time Series Analysis Package Integrated with the LiCSAR Automated Sentinel-1 InSAR Processor. Remote Sens 12:424.

https://doi.org/10.3390/rs12030424

Nakagawa R, Fukushima Y, Kano M, Yano K, Hirahara K, Tanaka Y, Okada Y (2024) Aseismic fault slip estimation from GNSS displacements using model-supervised deep neural interpolator. In: Abstract of 2024 Fall Meeting, American Geophysical Union, Washington D.C., 9–13 December 2024.

Nishimura T (2014) Short-term slow slip events along the Ryukyu Trench, southwestern Japan, observed by continuous GNSS. Progress in Earth and Planetary Science 1:1–13. https://doi.org/10.1186/s40645-014-0022-5

Nishimura T, Matsuzawa T, Obara K (2013) Detection of short-term slow slip events along the Nankai Trough, southwest Japan, using GNSS data. J Geophys Res Solid Earth 118:3112–3125. https://doi.org/10.1002/jgrb.50222

Ohno K, Ohta Y, Kawamoto S, Abe S, Hino R, Koshimura S, Musa A, Kobayashi H (2021) Real-time automatic uncertainty estimation of coseismic single rectangular fault model using GNSS data. Earth Planets Space 73:1–18. https://doi.org/10.1186/s40623-021-01425-0

Okada Y (1992) Internal deformation due to shear and tensile faults in a half-space. Bull Seismol Soc Am 82:1018–1040. https://doi.org/10.1785/BSSA0820021018

Okada Y, Fukushima Y (2026) Programs used in "Deep-learning-based denoising and interpolation of small displacements caused by fault slip using InSAR and GNSS data: Application to the 2019 Mw 6.2 Hyuga-nada earthquake" (Version 1.0.0) [Computer software]. Zenodo. https://doi.org/10.5281/zenodo.21897538

Okada Y, Nishimura T (2023) Systematic detection of short‐term slow slip events in southcentral Alaska. Geophys Res Lett 50: e2023GL104901. https://doi.org/10.1029/2023gl104901

Okada Y, Nishimura T (2025) Investigation on short-term slow slip events in the northeast Japan subduction zones using decadal GNSS data. Earth Planets Space 77:45. https://doi.org/10.1186/s40623-025-02175-z

Okada Y, Nishimura T, Tabei T, Matsushima T, Hirose H (2022) Development of a detection method for short-term slow slip events using GNSS data and its application to the Nankai subduction zone. Earth Planets Space 74:1–18. https://doi.org/10.1186/s40623-022-01576-8

Okada Y, Ueda T (2025) Development of a Seasonal Adjustment Technique STEL and its Application to Daily GNSS Data. Journal of the Geodetic Society of Japan 71:1–11. https://doi.org/10.11366/sokuchi.71.1 (In Japanese)

Okur Y, Fukushima Y, Ching K-E, Sharma Y (2025) Interactions of aseismic and seismic slips of the Philippine Fault on Leyte Island revealed by InSAR and GNSS time-series. Prog Earth Planet Sci 12:93. https://doi.org/10.1186/s40645-025-00758-8

Ozawa T, Shimizu S (2010) Atmospheric noise reduction in InSAR analysis using numerical weather model. Journal of the Geodetic Society of Japan 56:137–147. https://doi.org/10.11366/sokuchi.56.137 (In Japanese)

Park S, Avouac J-P, Zhan Z, Gualandi A (2023) Weak upper-mantle base revealed by postseismic deformation of a deep earthquake. Nature 615:455–460. https://doi.org/10.1038/s41586-022-05689-8

Rouet-Leduc B, Jolivet R, Dalaison M, Johnson PA, Hulbert C (2021) Autonomous extraction of millimeter-scale deformation in InSAR time series using deep learning. Nat Commun 12:6480. https://doi.org/10.1038/s41467-021-26254-3

Rousset B, Bürgmann R, Campillo M (2019) Slow slip events in the roots of the San Andreas fault. Sci Adv 5:eaav3274. https://doi.org/10.1126/sciadv.aav3274

Rousset B, Campillo M, Lasserre C, Frank WB, Cotte N, Walpersdorf A, Socquet A, Kostoglodov V (2017) A geodetic matched filter search for slow slip with application to the Mexico subduction zone. J Geophys Res Solid Earth 122:10,498-10,514. https://doi.org/10.1002/2017JB014448

Rousset B, Jolivet R, Simons M, Lasserre C, Rlel B, Milillo P, Çaklr Z, Renard F (2016) An aseismic slip transient on the North Anatolian Fault. Geophys Res

Lett 43:3254–3262. https://doi.org/10.1002/2016GL068250

Sagiya T, Thatcher W (1999) Coseismic slip resolution along a plate boundary megathrust: The Nankai Trough, southwest Japan. J Geophys Res 104:1111–1129. https://doi.org/10.1029/98JB02644

Schwegmann CP, Kleynhans W, Engelbrecht J, Mdakane LW, Meyer RGV (2017) Subsidence feature discrimination using deep convolutional neural networks in synthetic aperture radar imagery. In: 2017 IEEE International Geoscience and Remote Sensing Symposium (IGARSS). IEEE, pp 4626–4629

Shen Z-K, Jackson DD, Ge BX (1996) Crustal deformation across and beyond the Los Angeles basin from geodetic measurements. J Geophys Res 101:27957–27980. https://doi.org/10.1029/96JB02544

Shibata R, Kubo H, Suzuki W, Aoi S, Sekiguchi H (2025) Source process estimation for the 2024 Mw 7.1 Hyuganada, Japan, earthquake and forward modeling using N ‐ net ocean bottom seismometer data. Geophys Res Lett 52:e2025GL115401. https://doi.org/10.1029/2025GL115401

Takamatsu N, Muramatsu H, Abe S, Hatanaka Y, Furuya T, Kakiage Y, Ohashi K, Kato C, Ohno K, Kawamoto S (2023) New GEONET analysis strategy at GSI: daily coordinates of over 1300 GNSS CORS in Japan throughout the last quarter century. Earth Planets Space 75:1–19. https://doi.org/10.1186/s40623-023-01787-7

Tanaka Y, Kano M, Yano K (2025) Detecting slow slip signals in southwest Japan based on machine learning trained by real GNSS time series. J Geophys Res Solid Earth 130: e2024JB029499. https://doi.org/10.1029/2024jb029499

Usui Y, Aoki S, Hayashimoto N, Shimoyama T, Nozaka D, Yoshida T (2010) Description of and Advances in Automatic CMT Inversion Analysis. Quarterly Journal of Seismology 73:169–184

Vaswani A, Shazeer N, Parmar N, Uszkoreit J, Jones L, N.Gomez A, Kaiser L, Polosukhin I (2025) Attention is all you need. arXiv:1706.03762v7.

https://doi.org/10.48550/arXiv.1706.03762

Wang K, Fialko Y (2018) Observations and modeling of coseismic and postseismic deformation due to the 2015 Mw 7.8 Gorkha (Nepal) earthquake. J Geophys Res Solid Earth 123:761–779

Weston, J., Ferreira A. M. G., Funning G. J. (2011) Global compilation of interferometric synthetic aperture radar earthquake source models: 1. Comparisons with seismic catalogs, Journal of Geophysical Research 116, B08408. https://doi.org/10.1029/2010JB008131.

Wdowinski S, Bock Y, Zhang J, Fang P, Genrich J (1997) Southern California permanent GPS geodetic array: Spatial filtering of daily positions for estimating coseismic and postseismic displacements induced by the 1992 Landers earthquake. Journal of Geophysical Research 102:17659–18517. https://doi.org/10.1029/97JB01378

Xue X, Freymueller J. T. (2023) Machine learning for single - station detection of transient deformation in GPS time series with a case study of Cascadia slow slip. J Geophys Res Solid Earth 128: e2022JB024859. https://doi.org/10.1029/2022jb024859

Yagi Y, Kikuchi M, Sagiya T (2001) Co-seismic slip, post-seismic slip, and aftershocks associated with two large earthquakes in 1996 in Hyuga-nada, Japan. Earth Planets Space 53:793–803. https://doi.org/10.1186/BF03351677

Yagi Y, Kikuchi M, Yoshida S, Sagiya T (1999) Comparison of the coseismic rupture with the aftershock distribution in the Hyuga-nada Earthquakes of 1996. Geophys Res Lett 26:3161–3164. https://doi.org/10.1029/1999GL005340

Yamamoto Y, Obana K, Takahashi T, Nakanishi A, Kodaira S, Kaneda Y (2013) Imaging of the subducted Kyushu-Palau Ridge in the Hyuga-nada region, western Nankai Trough subduction zone. Tectonophysics 589:90–102. https://doi.org/10.1016/j.tecto.2012.12.028

Yamashita Y, Shinohara M, Yamada T (2021) Shallow tectonic tremor activities in

Hyuga-nada, Nankai subduction zone, based on long-term broadband ocean bottom seismic observations. Earth Planets Space 73:196. https://doi.org/10.1186/s40623-021-01533-x

Yamashita Y, Yakiwara H, Asano Y, Shimizu H, Uchida K, Hirano S, Umakoshi K, Miyamachi H, Nakamoto M, Fukui M, et al (2015) Migrating tremor off southern Kyushu as evidence for slow slip of a shallow subduction interface. Science 348:676–679. https://doi.org/10.1126/science.aaa4242

Yano K, Kano M (2022) l_1 trend filtering‐based detection of short‐term slow slip events: Application to a GNSS array in southwest Japan. J Geophys Res Solid Earth 127: e2021JB023258. https://doi.org/10.1029/2021jb023258

Yarai H, Ozawa S (2013) Quasi-periodic slow slip events in the afterslip area of the 1996 Hyuga-nada earthquakes, Japan. J Geophys Res Solid Earth 118:2512–2527. https://doi.org/10.1002/jgrb.50161

Yu C, Li Z, Penna NT, Crippa P (2018) Generic atmospheric correction model for interferometric synthetic aperture radar observations. J Geophys Res Solid Earth 123:9202–9222. https://doi.org/10.1029/2017JB015305

Zhang X, Li S, Chen L (2025) Unexpected megathrust slip evolution revealed by the 2024 Mw 7.1 and the 2025 Mw 6.8 Hyuga-nada earthquakes in southwest Japan. Earth Planet Sci Lett 662:119384. https://doi.org/10.1016/j.epsl.2025.119384

Zhu C, Li X, Wang C, Zhang B, Li B (2024) Deep learning-based coseismic deformation estimation from InSAR interferograms. IEEE Trans Geosci Remote Sens 62:1–10. https://doi.org/10.1109/TGRS.2024.3357190

Zhu XX, Montazeri S, Ali M, Hua Y, Wang Y, Mou L, Shi Y, Xu F, Bamler R (2021) Deep Learning Meets SAR: Concepts, models, pitfalls, and perspectives. IEEE Geosci Remote Sens Mag 9:143–172. https://doi.org/10.1109/MGRS.2020.3046356

Figure 1. Tectonic setting in the target area. Red lines indicate iso-slip contours of the 1944 Tonankai and 1946 Nankai earthquakes (Sagiya and Thatcher 1999), starting at 1 m with an interval of 1 m. "KPR" stands for Kyushu-Palau ridge, and blue dashed lines denote its subducted part (Yamamoto et al. 2013). **(a)** Regional map of the analysis region. **(b)** Major megathrust earthquake distribution in the Hyuga-nada area. Orange, gold, pink, and brown contours indicate the slip area of the October 1996, December 1996, August 2024, and January 2025 earthquakes, respectively (Yagi et al. 1999; Itoh 2025; Zhang et al. 2025). A "beachball" denotes the centroid moment tensor (CMT) of the May 2019 earthquake retrieved from the Japan Meteorological Agency (JMA) (Usui et al. 2010). Gray arrows indicate SAR satellite information: the longer arrow shows the flight direction, and the shorter arrow shows the look direction.

Figure 2. Outline of the proposed model architecture.

Figure 3. Example of signals and noises in the synthetic InSAR data. The look direction is the same as that shown in Figure 1b. (a) Ground truth line-of-sight (LOS) displacement field. The pink rectangle indicates the assumed fault plane. (b) Topography-correlated noise. (c) Long-wavelength noise. (d) Spatially-correlated random noise. (e) Decorrelation noise. (f) Synthetic InSAR data, created by the stacking of (a) – (e).

Figure 4. GNSS station distribution and example of synthetic GNSS data. **(a)** GNSS stations used in this study. **(b)** Synthetic GNSS time series. Triangles, diamonds, and circles indicate east-west (EW), north-south (NS), and up-down (UD) components of GNSS data, respectively. Pink and blue symbols denote data at 021084 and 021090, respectively.

Figure 5. Application result of the trained model to synthetic data. **(a)**, **(b)**, and **(c)** show the ground truth of EW, NS, and UD components, respectively. The color of the squares indicates the pseudo-observation displacement at GNSS stations. **(d)**, **(e)**, and **(f)** show the inferred displacement fields of the EW, NS, and UD components, respectively. **(g)**, **(h)**, and **(i)** show residual displacements between the estimates and ground truth of the EW, NS, and UD components, respectively.

Figure 6. Distribution of VRs for each component. **(a)** Two-dimensional histogram of VRs for the EW component. Pink dots indicate the mean VRs for each displacement range. Gray lines indicate the mean noise levels of the horizontal component of GNSS data (denoted as GNSS-H), the vertical component of GNSS data (denoted as GNSS-V), and InSAR data. **(b)** Same as (a) but at the NS component. **(c)** Same as (a) but at the UD component.

Figure 7. Comparison of model performance between the joint and GNSS-only models. **(a)** Comparison of VRs for the EW component. Red circles and blue squares indicate the mean VRs for the joint and GNSS-only models, respectively. Error bars denote the one-sigma interval of the mean VR based on the standard deviation. Gray lines indicate the mean noise level of the horizontal component of GNSS data (denoted as GNSS-H), the vertical component of GNSS data (denoted as GNSS-V), and InSAR data. **(b)** Same as (a) but for the NS component. **(c)** Same as (a) but for the UD component.

Figure 8. Application result of the CNN model to the observed InSAR and GNSS data, including the coseismic displacements of the 2019 Hyuga-nada earthquake. (**a**) EW, (**b**) NS, and (**c**) UD components.

Figure 9. Source model estimation result using the denoised displacement fields. Black dashed lines indicate the iso-depth contours of the Philippine Sea plate interface between 10 and 50 km with an interval of 10 km. A pink square denotes the estimated fault model. (**a**)–(**c**) Denoised, in other words, input displacement fields of (a) EW, (b) NS, and (c) UD components. (**d**)–(**f**) Predicted displacements from the source model of (d) EW, (e) NS, and (f) UD components. (**g**)–(**i**) Residual between the inputs and predictions of (g) EW, (h) NS, and (i) UD components.

Figure 10. Comparison of the estimated source model with megathrust earthquakes and tectonic tremors. Black dashed lines indicate the iso-depth contours of the slab between 10 and 50 km with an interval of 10 km. A pink rectangle denotes the fault plane of the 2019 earthquake estimated in this study. A "beachball" denotes the CMT of the May 2019 earthquake provided by the JMA (Usui et al. 2010). Pink circles indicate M_j 2.0+ interplate earthquakes (located within ±10 km of the slab interface model by Iwasaki et al. (2015)) extracted from the JMA catalog for the period from January 1995 to August 2025. Orange contours show the slip magnitude of the 1996 and 2024–2025 doublets (Yagi et al. 1999; Itoh 2025; Zhang et al. 2025) with an interval of 0.5 m. Cyan circles denote the epicenters of tectonic tremors (Yamashita et al. 2021).

List of additional files

Additional file 1

File format: pdf

Title: Additional file 1

Description: Supporting information of the main manuscript (Figures S1–S17 and Tables S1–S5).

Manuscript submitted to *EarthArXiv* as a non-peer-reviewed preprint
and also submitted for peer review to *Earth, Planets and Space*

Additional File 1

Deep-learning-based denoising and interpolation of small displacements caused by fault slip using InSAR and GNSS data: Application to the 2019 Mw 6.2 Hyuga-nada earthquake

Yutaro Okada & Yo Fukushima

Corresponding author: Yutaro Okada (yutaro.okada.c8@tohoku.ac.jp)

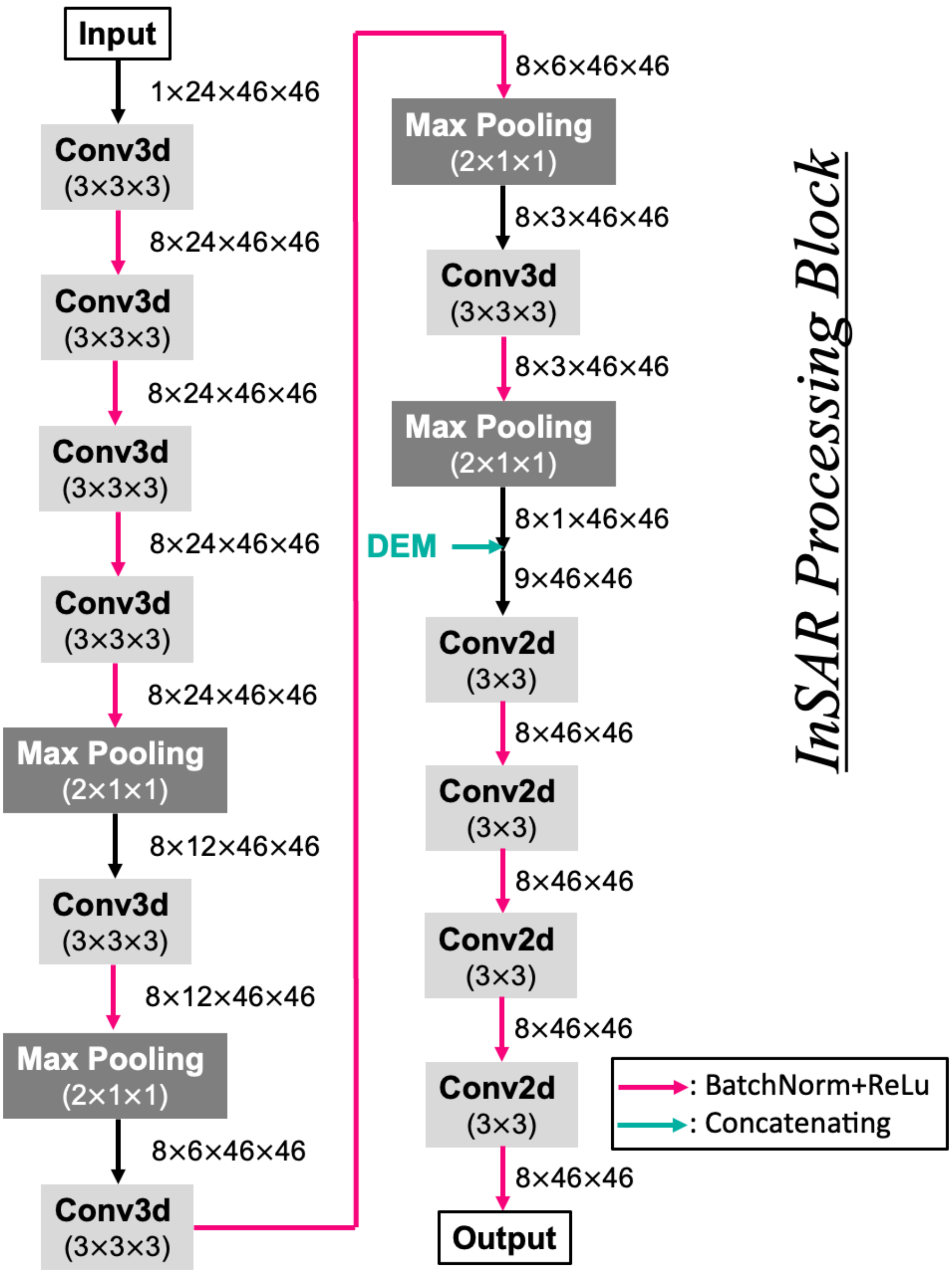

Figure S1. Architecture of the InSAR data processing part in the developed model. Numbers inside and outside of gray boxes denote the size of kernels and feature maps, respectively.

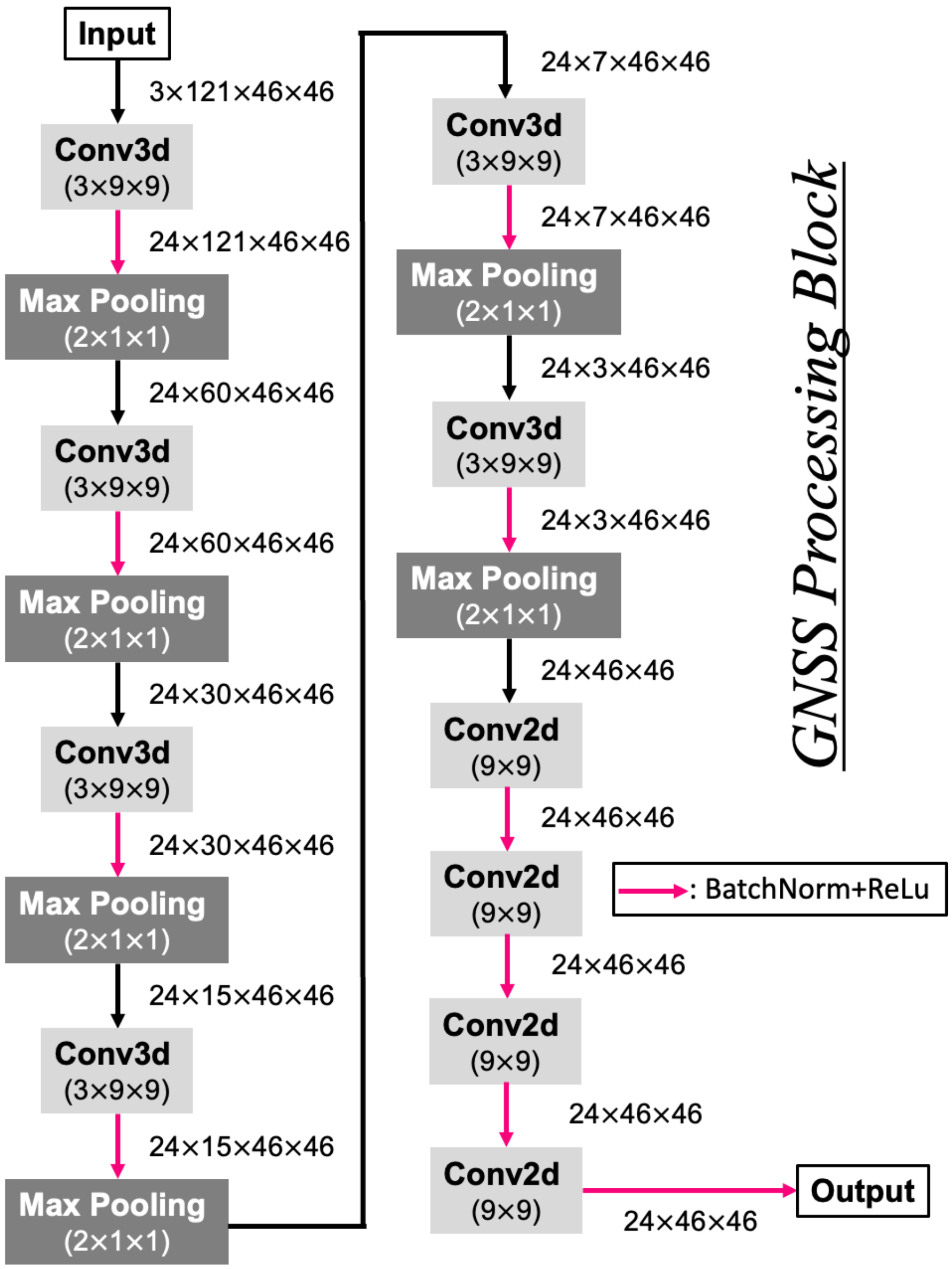

Figure S2. Same as Figure S1 but architecture of the GNSS data processing part in the developed model.

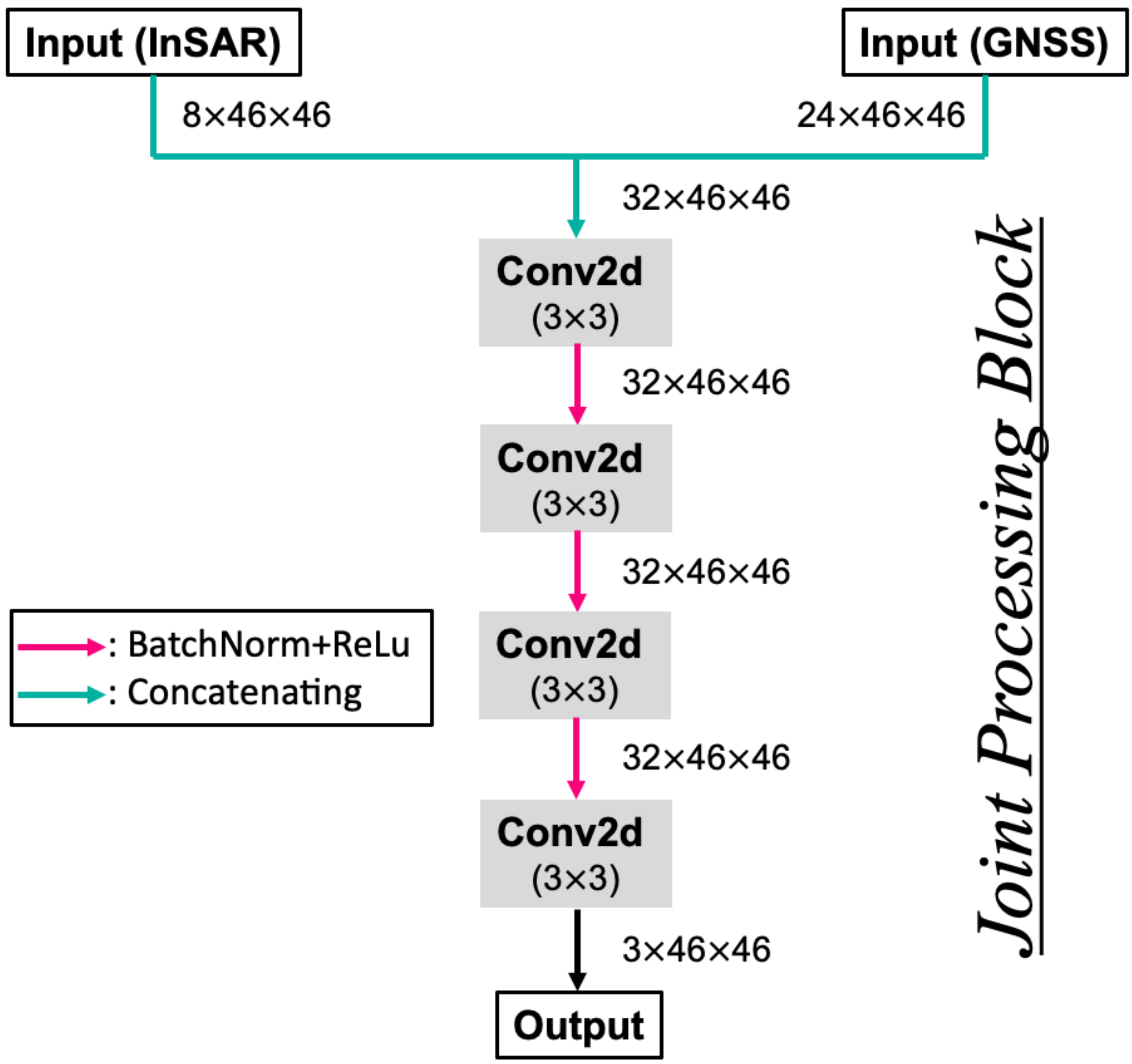

Figure S3. Same as Figure S1 but architecture of the joint processing part in the developed model.

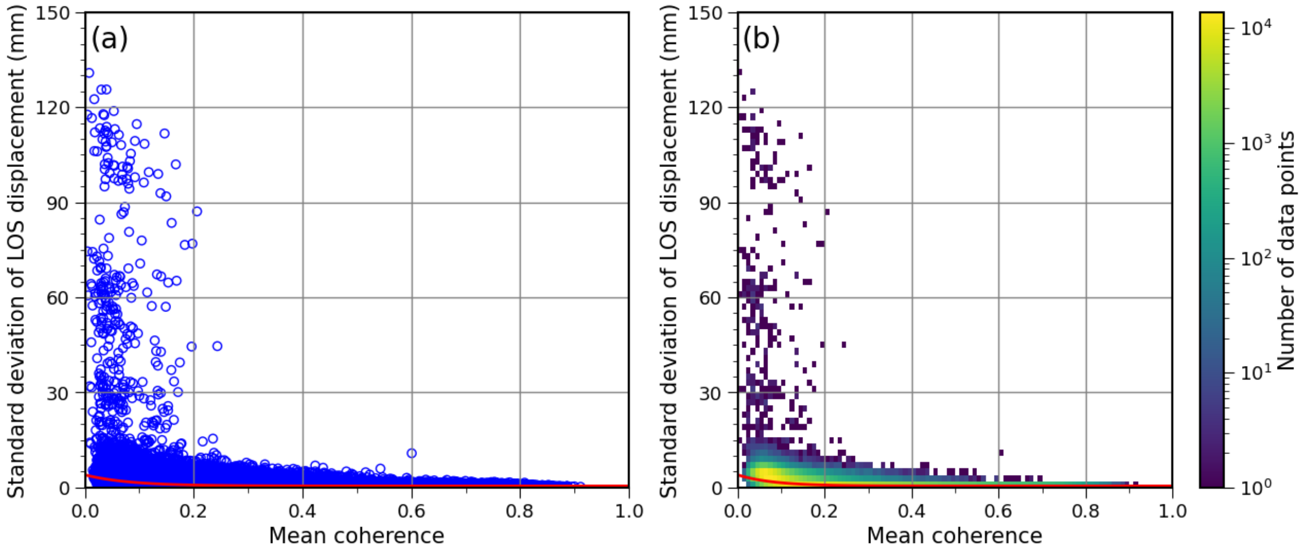

Figure S4. Relationship between the standard deviation of unwrapped displacements and coherence. The red line indicates the empirical model in Equation 9. **(a)** Scatter plot. **(b)** Two-dimensional histogram.

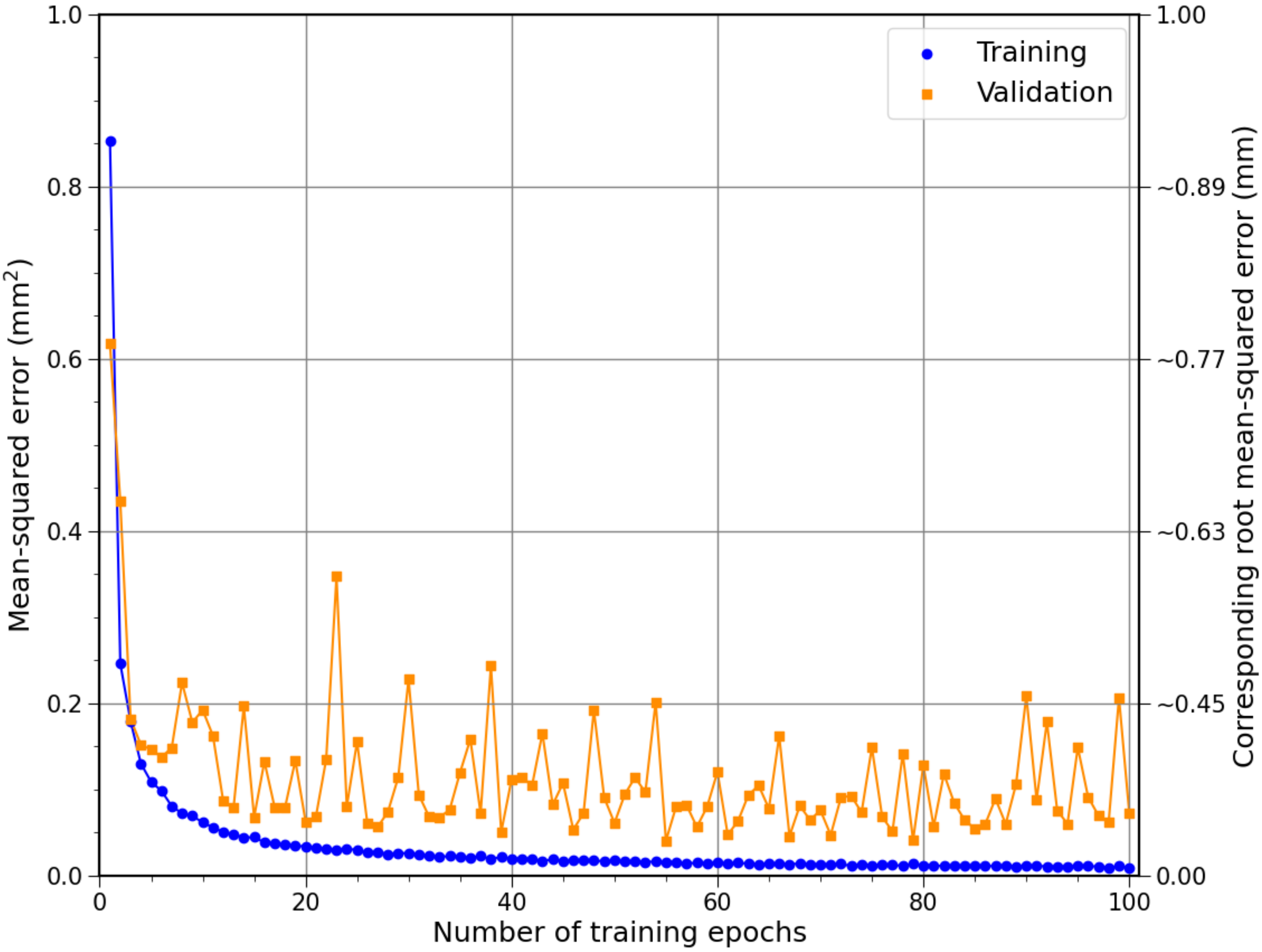

Figure S5. Loss curve for the training and validation of the proposed deep-learning model. Blue and orange symbols indicate average mean-squared errors for training and validation datasets, respectively. The y-axis in a light hand side shows the square root of the mean-squared error, i.e., the root mean-squared error, to compare with the noise level of the original datasets.

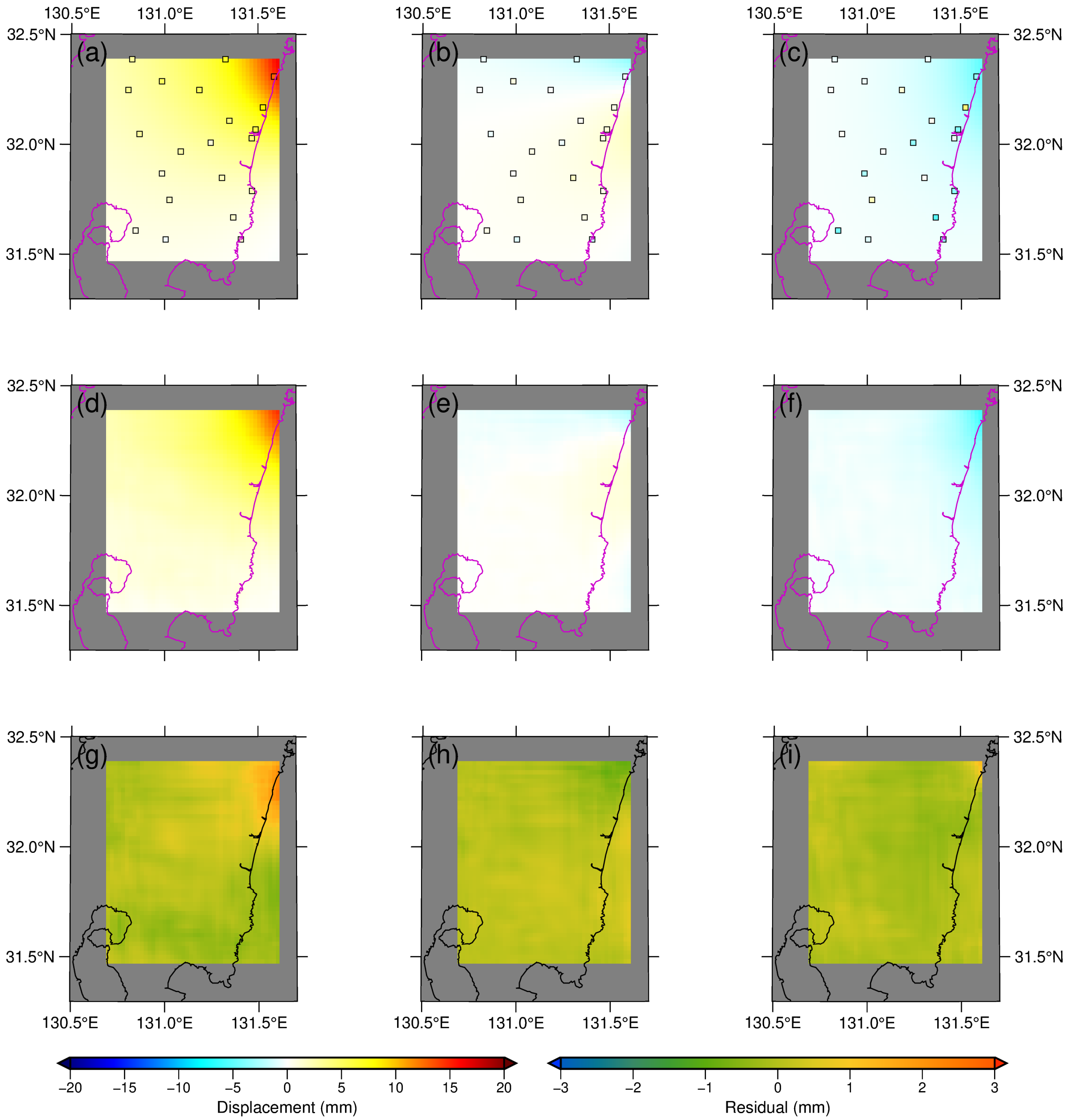

Figure S6. Example of an application result of the trained model to synthetic data. **(a)**, **(b)**, and **(c)** indicate the ground truth of east-west (EW), north-south (NS), and up-down (UD) components, respectively. The color of the squares indicates the displacement of pseudo-observation at GNSS stations. **(d)**, **(e)**, and **(f)** indicate the inferred displacement fields of EW, NS, and UD components, respectively. **(g)**, **(h)**, and **(i)** indicate residual displacements between the estimate and ground truth of EW, NS, and UD components, respectively.

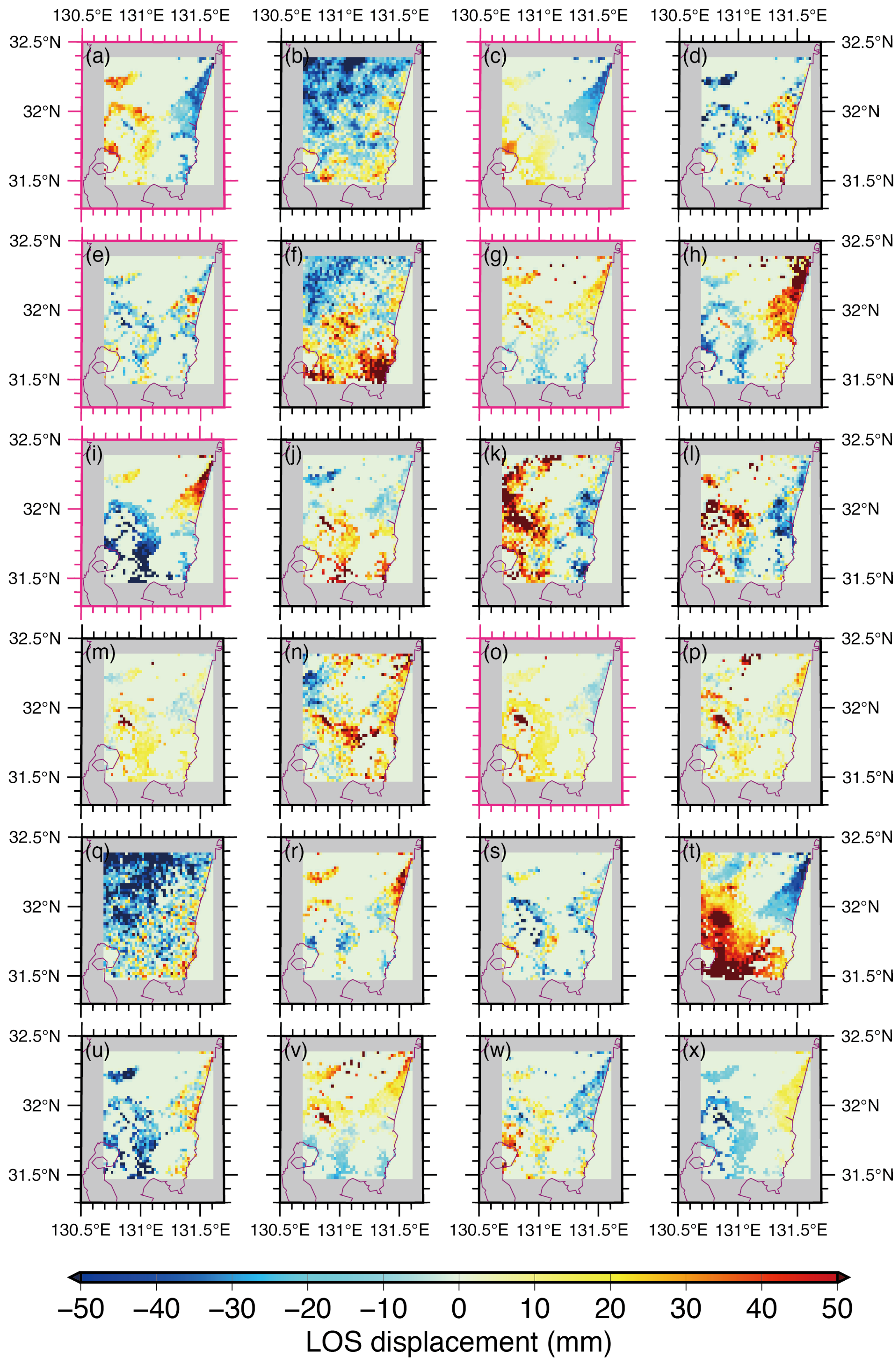

Figure S7. Synthetic InSAR dataset used for the case shown in Figure S6. Subplots with a pink frame show the interferogram recording coseismic displacements. A positive LOS displacement indicates shortening of the baseline.

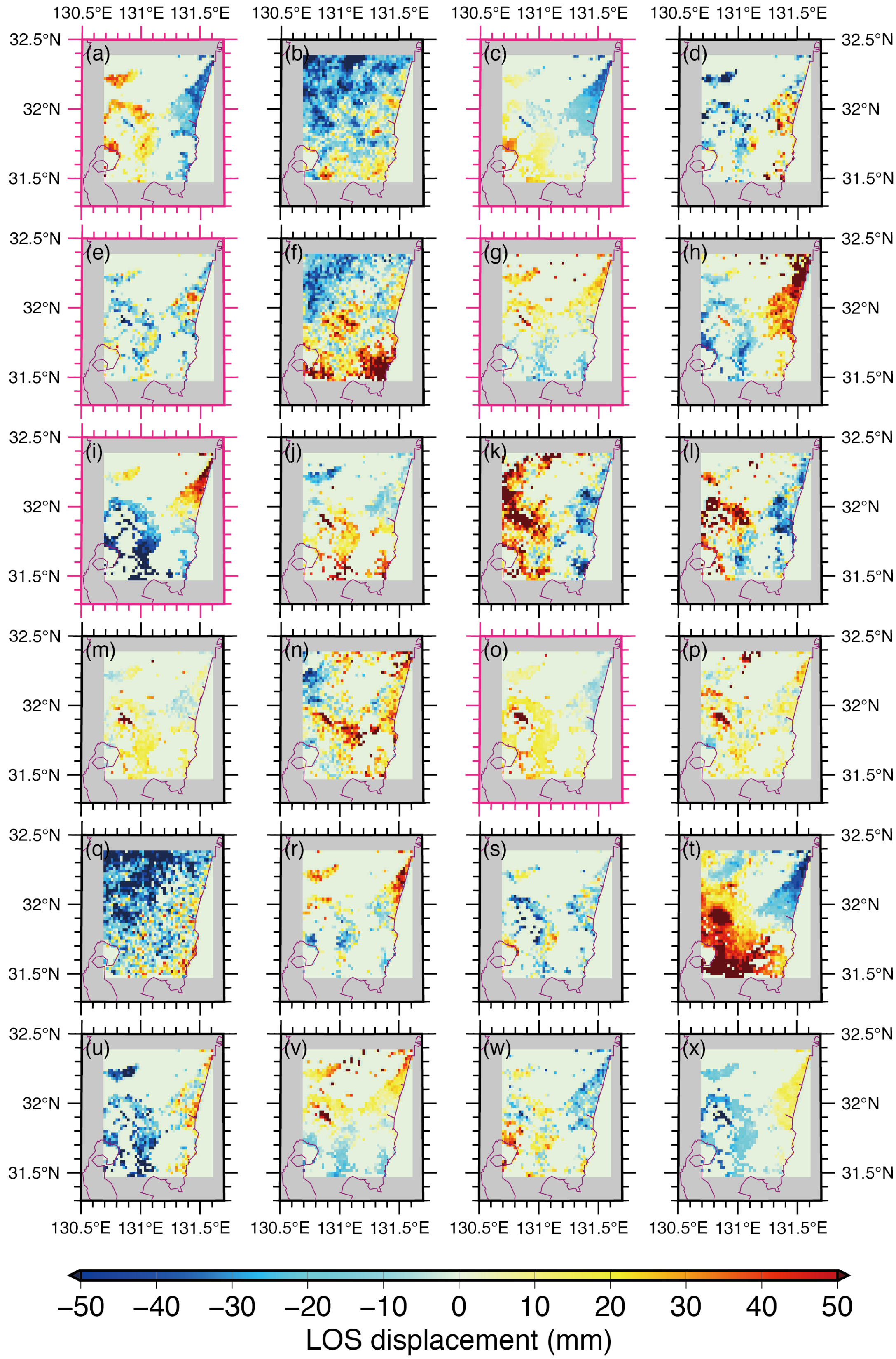

Figure S8. Synthetic InSAR dataset used for the case shown in Figure 5. Subplots with a pink frame show the interferogram recording coseismic displacements. A positive LOS displacement indicates shortening of the baseline.

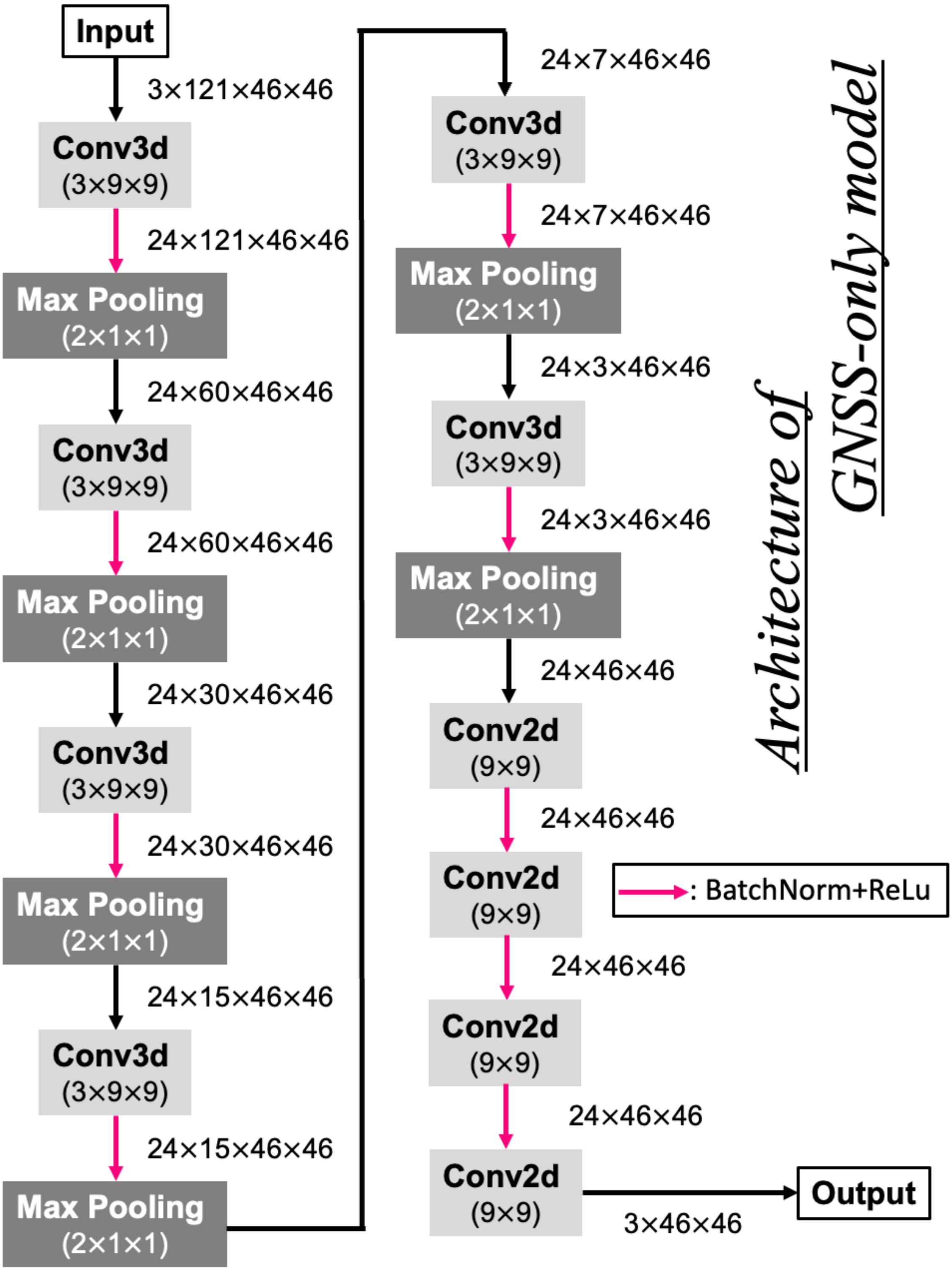

Figure S9. Same as Figure S1 but architecture of the alternative (GNSS-only) model.

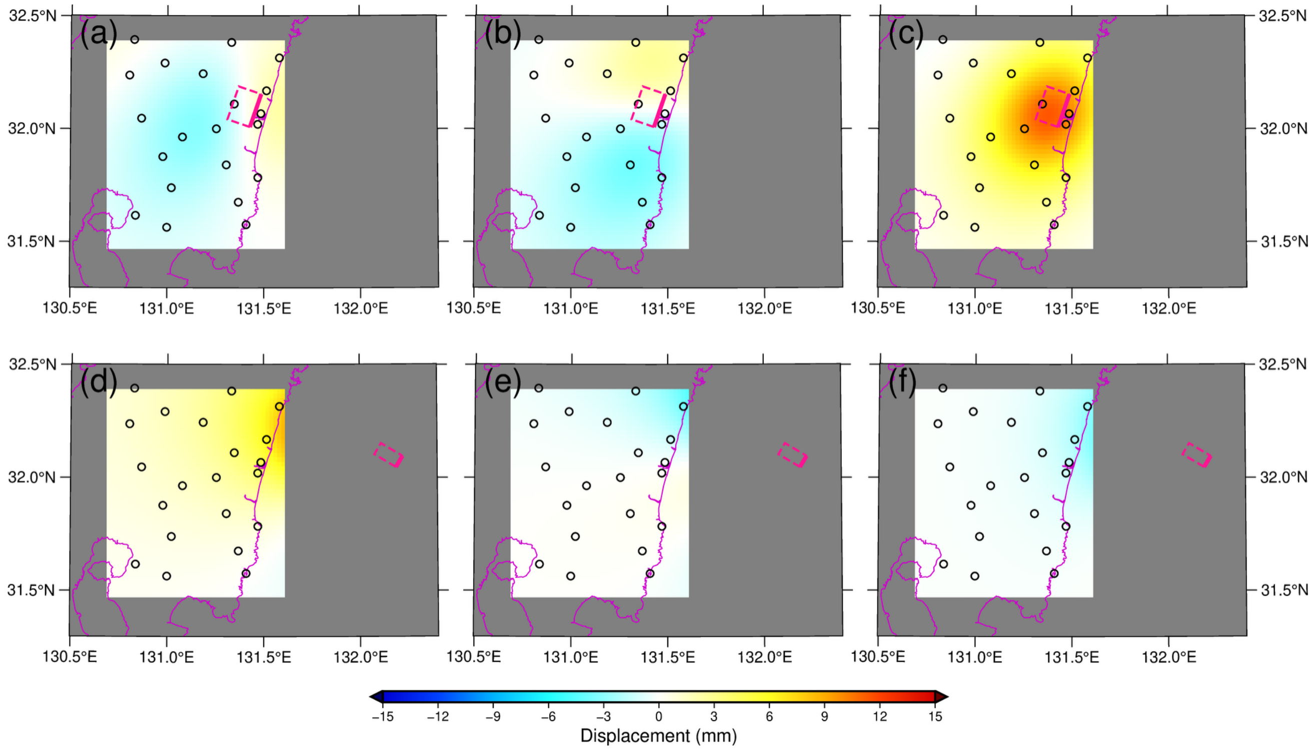

Figure S10. Synthetic displacement fields due to fault slip. (**a**) EW, (**b**) NS, and (**c**) UD components predicted from the reverse slip at the fault beneath the observation points. (**d**) EW, (**e**) NS, and (**f**) UD components predicted from the reverse slip at the fault away from the observation points. Cycles indicate the location of the GNSS stations.

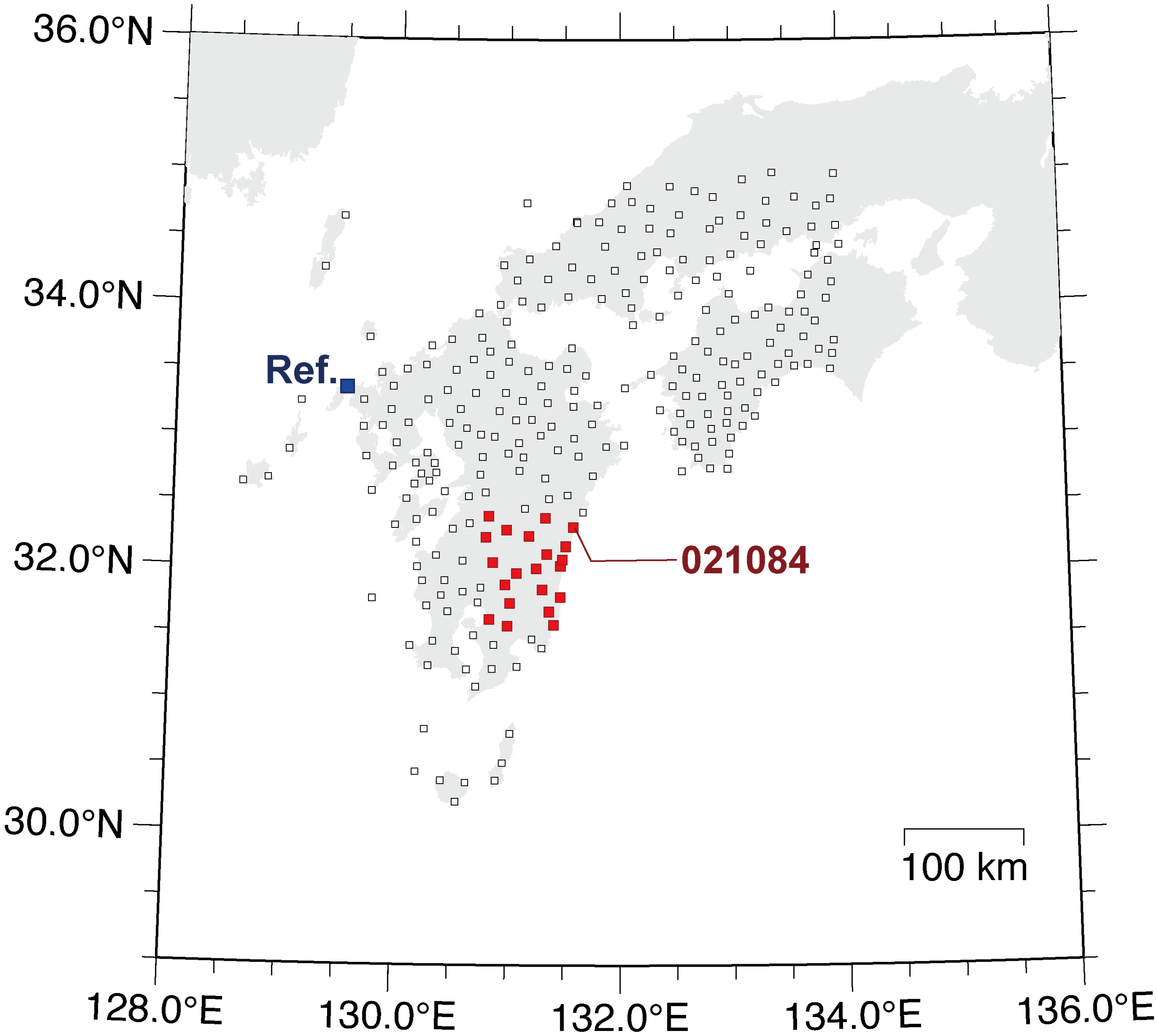

Figure S11. GNSS station map. White squares indicate the station used for the common-mode error estimation. A blue station denotes the reference station 950459. Red squares are the stations used for the main analysis.

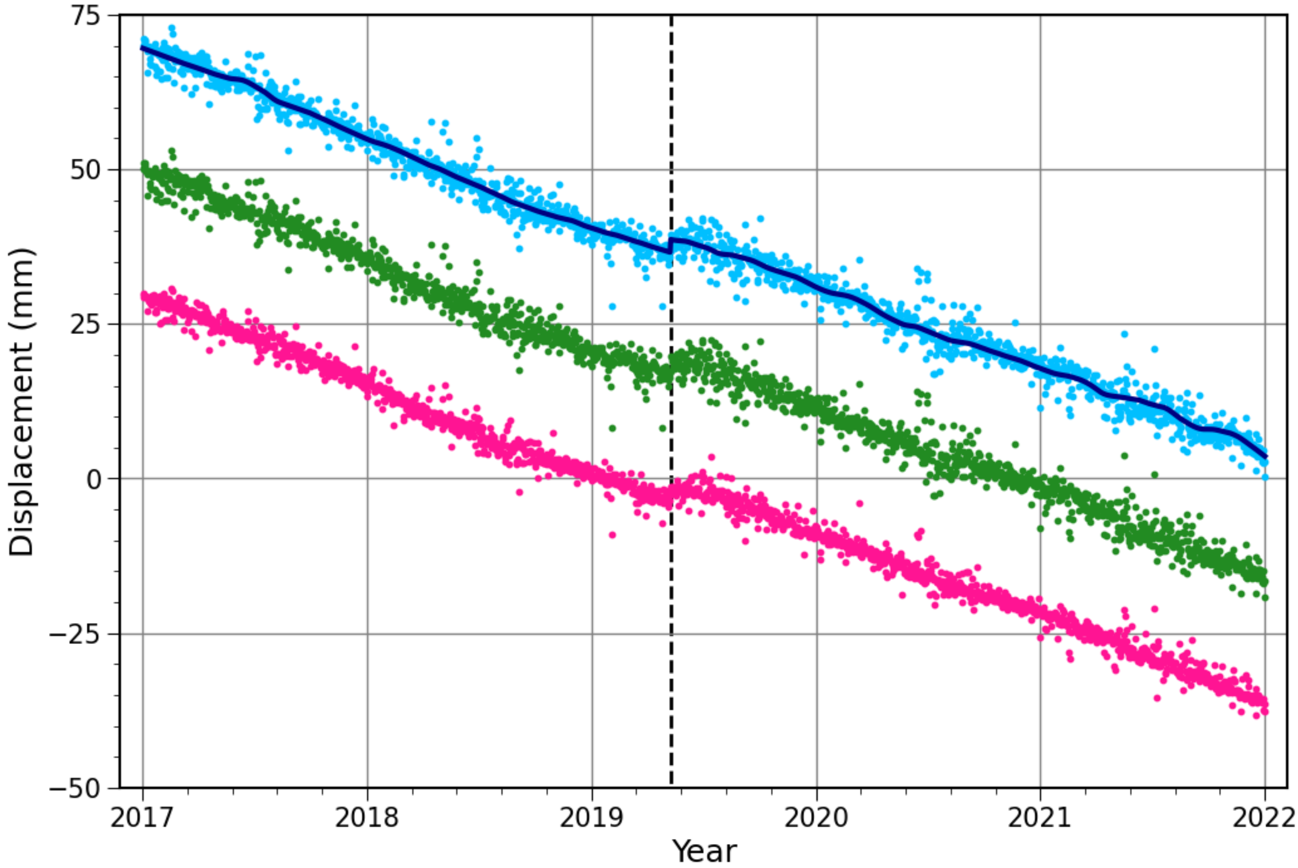

Figure S12. GNSS time series of the EW component of station 021084. Cyan, green, and pink time series denote GNSS data after referencing to 950459, after deseasonaling, and after the spatial filtering, respectively. The blue line indicates seasonal, trend, and episodic components modeled by the STEL. The black dashed line shows the timing of the target earthquake.

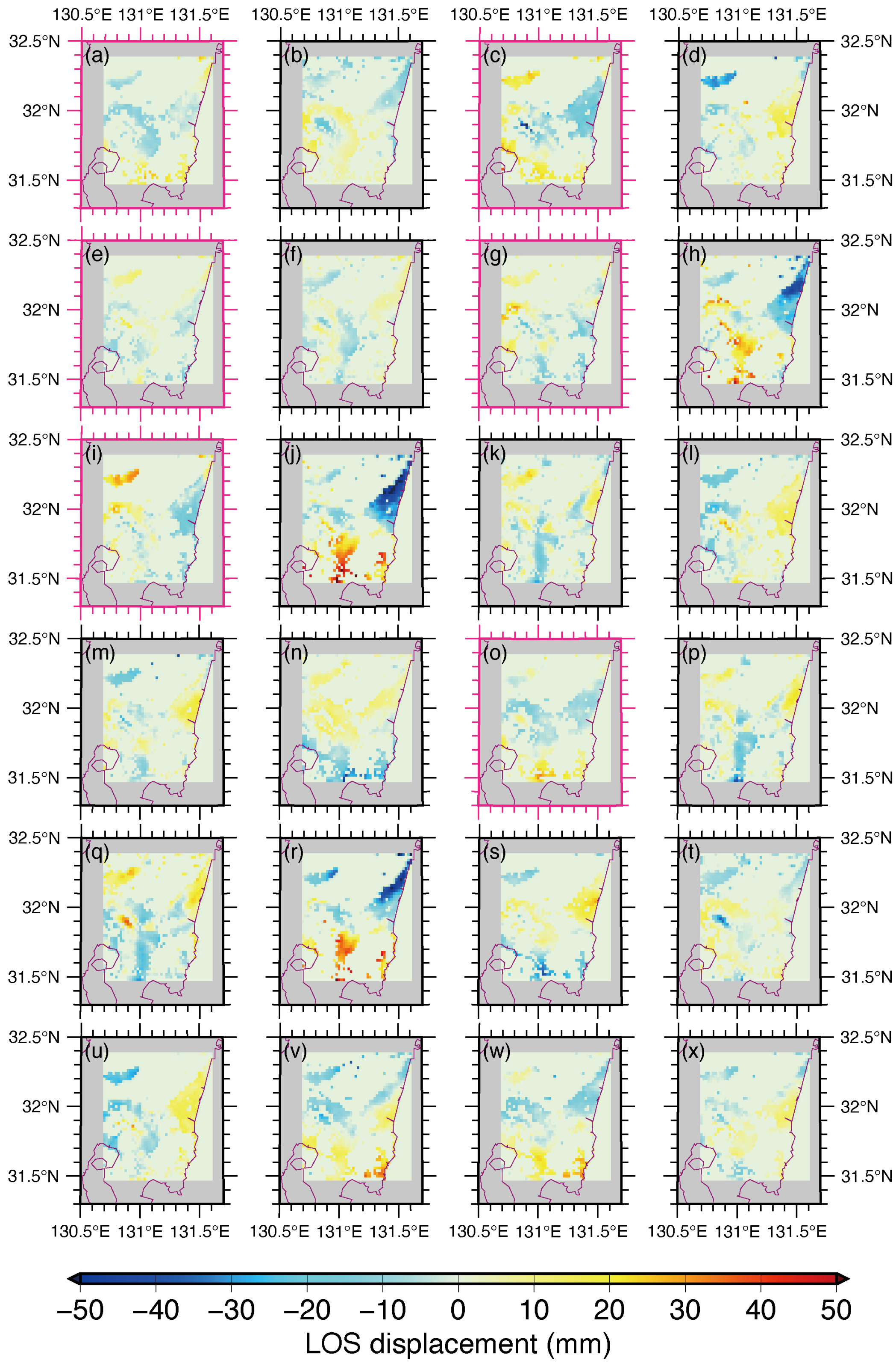

Figure S13. Observed InSAR dataset used for the case shown in Figure 8. Subplots with a pink frame show the interferogram recording coseismic displacements. A positive LOS displacement indicates shortening of the baseline.

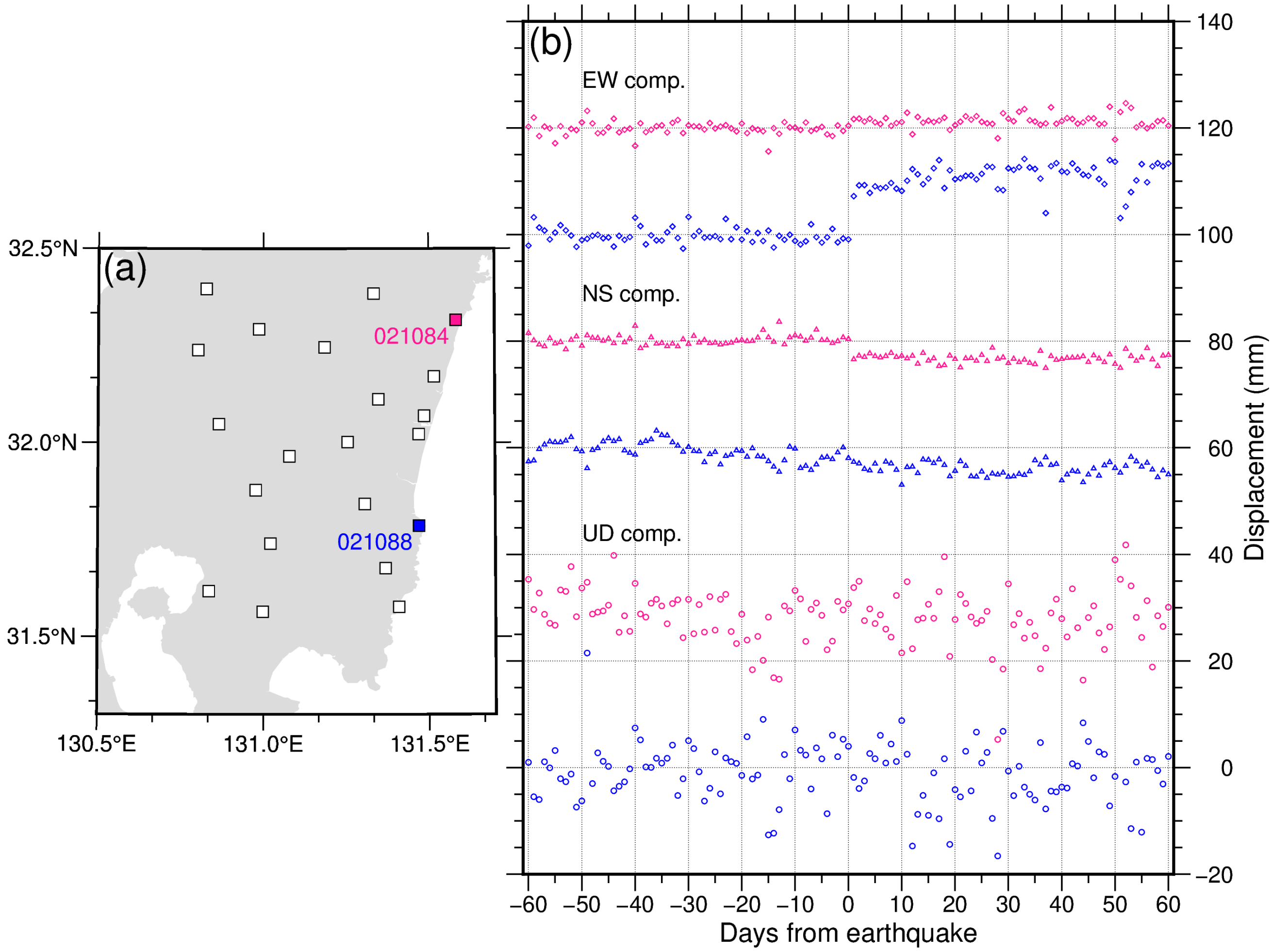

Figure S14. Observed GNSS time series used for the case shown in Figure 8. **(a)** Squares indicate GNSS stations. Time series of stations denoted by pink and blue are shown in (b). **(b)** Diamonds, triangles, and circles indicate EW, NS, and UD time series, respectively. Pink time series denotes positions of 021084, whereas blue time series shows positions of 021088.

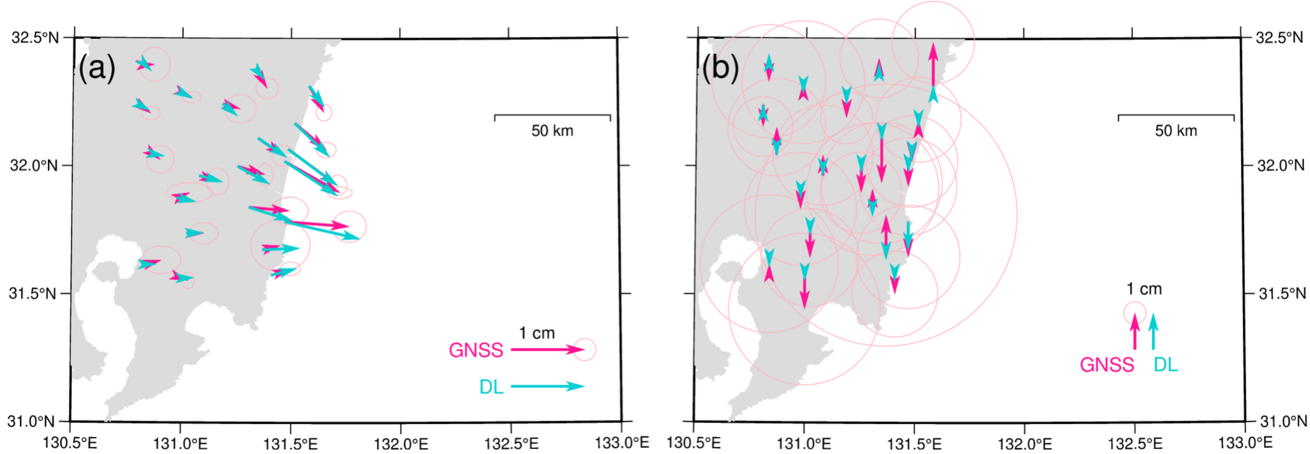

Figure S15. Comparison between the displacements computed from GNSS data (pink vectors) and those estimated by the deep-learning model (cyan vectors). Error ellipses indicate the 68% confidence interval of the observed displacements. (**a**) Horizontal and (**b**) vertical components.

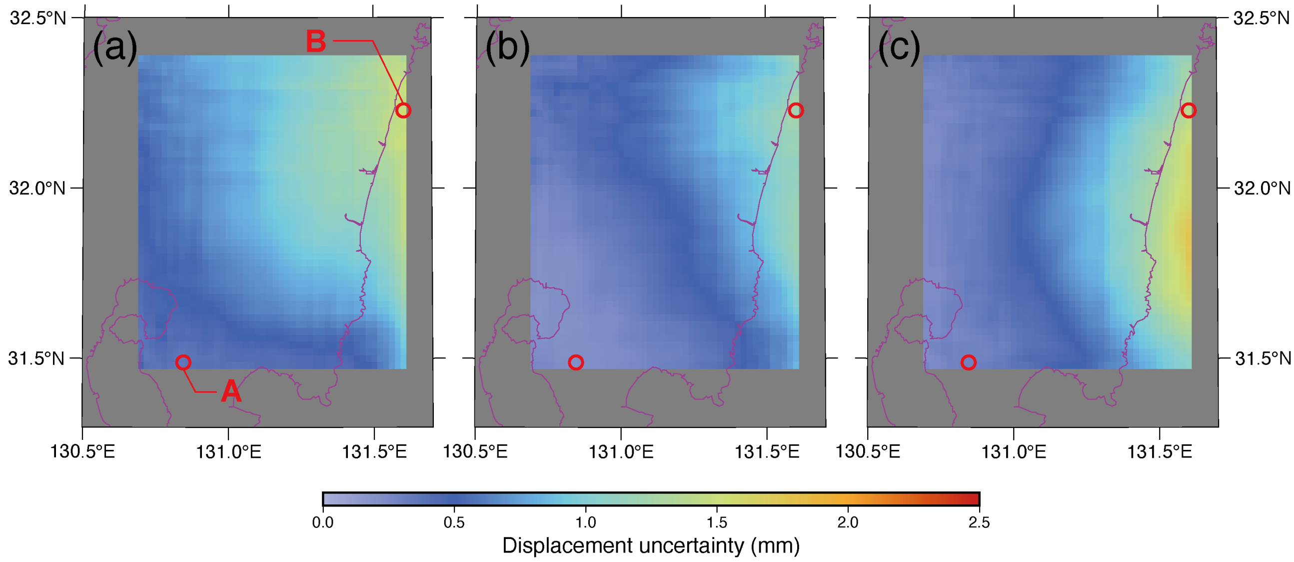

Figure S16. Uncertainty of the deep-learning result of (**a**) EW, (**b**) NS, and (**c**) UD components. Pink circles denote the pixels whose distribution of the squared residual is shown in Figure S17.

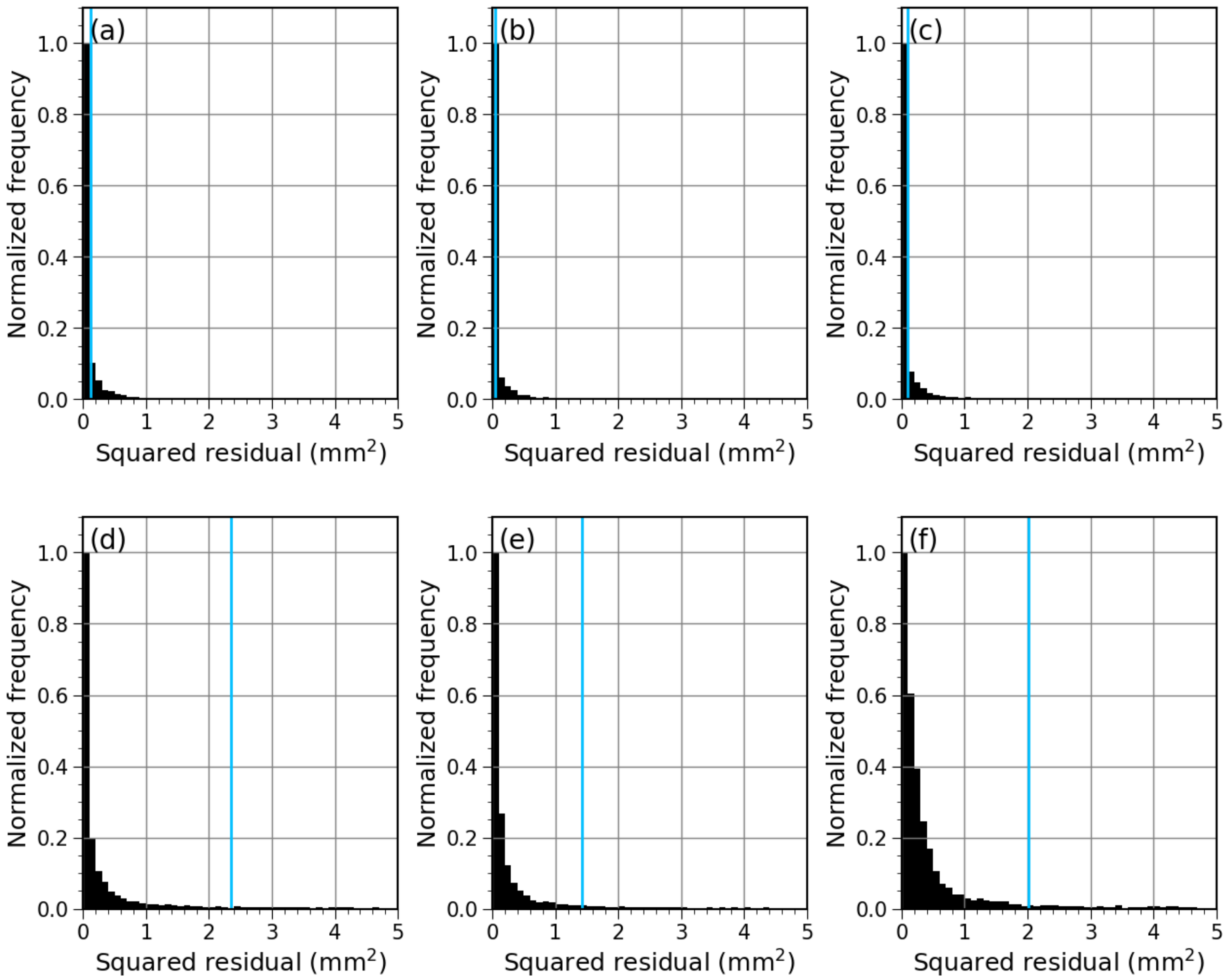

Figure S17. Frequency distribution of the squared residual at the selected pixels (Figure S16). The skyblue line indicates the truncated mean. Distribution of (**a**) EW, (**b**) NS, and (**c**) UD components at pixel A (Figure S16a). Distribution of (**d**) EW, (**e**) NS, and (**f**) UD components at pixel B (Figure S16a).

Table S1. Additional information for kernels

Part Name	Kernel Name	Padding		Stride	
		Space*	Time**	Space*	Time**
InSAR data processing part	Conv3d	1	1	1	1
	Max pooling	0	0	1	2
	Conv2d	1	N/A	1	N/A
GNSS data processing part	Conv3d	4	1	1	1
	Max pooling	0	0	1	2
	Conv2d	1	N/A	1	N/A
Joint processing part	Conv2d	1	N/A	1	N/A

*: Longitudinal and latitudinal directions

**: Time direction

Table S2. Range of parameters of a rectangular fault for generating ground truths

Parameter Name	Minimum	Maximum	Interval
Longitude (°)	130.5	133.5	0.1
Latitude (°)	31.5	32.5	0.1
Aspect ratio		0.5, 1, 2	
Stress drop (MPa)		1, 10, 100	
Slip direction (°)	115	135	10
Moment magnitude	5.5	7.5	0.1

Table S3. Earthquakes accounted for as the episodic component in the STEL decomposition

Date (UTC)	Longitude (°)	Latitude (°)	Depth (km)	M_j
April 8, 2018	132.5867	35.1847	12.13	6.1
January 8, 2019	131.1645	30.5725	30.05	6.0
May 9, 2019	131.9745	31.8012	25.46	6.3

Table S4. Parameter search range in the source model estimation

Parameter Name	Minimum	Maximum	Interval
Longitude (°)*	131.5	132.5	0.1
Latitude (°)*	31.2	32.2	0.1
Width (km)	5	105	5
Aspect ratio	1.0	3.0	0.5
Moment magnitude	5.5	7.0	0.1
Rake (°)	30	150	5

*: Center of the fault plane

Table S5. Estimated source model parameters

Parameter Name	Optimal value
Longitude (°)	132.0
Latitude (°)	31.7
Depth (km)	19.7
Length (km)	5.0
Width (km)	5.0
Strike (°)	206
Dip (°)	14
Rake (°)	75
Slip (m)	7.079